Materials & Design 267 (2026) 116332

Contents lists available at ScienceDirect

Materials & Design

journal homepage: www.elsevier.com/locate/matdes

Influence of local thermal conditions on solidification patterns in laser beam welding: An experimentally aided phase-field study

Muhammad Umar[a, b, *], Ahmed Elmoghazy[a], Andrey Gumenyuk[e], Nasim Bakir[d], Daniel Schneider[a, b, c], Britta Nestler[a, b, c], Michael Rethmeier[d, e, f], Michael Schmidt[g, h]

[a] Institute of Applied Materials (IAM-MMS), Karlsruhe Institute of Technology, Kaiserstrasse 12, Karlsruhe, 76131, Baden-Württemberg, Germany
[b] Institute of Digital Materials Science (IDM), Karlsruhe University of Applied Sciences, Moltkestr. 30, Karlsruhe, 76133, Baden-Württemberg, Germany
[c] Institute of Nanotechnology (INT), Karlsruhe University of Applied Science, Moltkestr. 30, Karlsruhe, 76133, Baden-Württemberg, Germany
[d] Institut für Werkzeugmaschinen und Fabrikbetrieb (IWF), Technische Universität Berlin, Pascalstraße 8 - 9, Berlin, 10587, Berlin, Germany
[e] Bundesanstalt für Materialforschung und -prüfung (BAM), 9.3 Welding Technology, Unter den Eichen 87, Berlin, 12205, Berlin, Germany
[f] Fraunhofer-Institut Produktionsanlagen und Konstruktionstechnik (IPK), Pascalstraße 8 - 9, Berlin, 10587, Berlin, Germany
[g] Institute of Photonic Technologies (LPT), Friedrich-Alexander-Universität Erlangen-Nürnberg, Konrad-Zuse-Straße 3/5, Erlangen, 91052, Bavaria, Germany
[h] Erlangen Graduate School in Advanced Optical Technologies (SAOT), Friedrich-Alexander-Universität Erlangen-Nürnberg, Paul-Gordan-Straße 6, Erlangen, 91052, Bavaria, Germany

ARTICLE INFO

Keywords:
Dendritic solidification
Laser beam welding
Quaternary EN1.4301 alloy
Finite element analysis
Phase-field simulations
Kadi4Mat workflow

ABSTRACT

Solidification cracking in laser beam welding (LBW) is governed by local thermal conditions at the weld-pool boundary, yet the sub-micron microstructural response across the full mushy zone remains poorly understood. This study employs an automated phase-field (PF) simulation workflow, integrated within the Kadi4Mat research data management platform, to conduct a systematic, FAIR-compliant parametric study of dendritic solidification in the quaternary EN 1.4301 (Fe–Cr–Ni–C) alloy. Thermal conditions—thermal gradient (G), solidification velocity (V_s), and grain misorientation angle (θ_R)—are extracted from a thermocouple-validated ANSYS Fluent weld-pool model and used as inputs to 2D and 3D PACE3D phase-field simulations spanning G from 100 to 900 K/mm, V_s from 5 to 40 mm/s, and θ_R from 0° to 45°. Key findings demonstrate that θ_R is a critical parameter—alongside G and V_s—governing the cellular-to-dendritic morphological transition, secondary dendrite arm formation, and the topology of inter-dendritic liquid (continuous films versus isolated pockets), each carrying distinct solidification cracking risk pathways. The Kadi4Mat workflow reduces manual pre-processing effort substantially while ensuring data reproducibility and reuse. Quantitative validation against electron probe micro-analysis confirms primary dendrite arm spacing predictions within 12% at the upper weld surface and within 4% at the mid-section.

1. Introduction

Laser beam welding (LBW) is a high-precision joining technology widely deployed in automotive, aerospace, and energy sectors, prized for its deep penetration capability, narrow heat-affected zone, and high throughput [1]. A critical obstacle to its broad industrial adoption, however, is solidification cracking (SC)—a hot-cracking defect that initiates at the weld centerline during the final stage of solidification and can compromise structural integrity under service loading. The root causes of SC are microstructural: the topology of inter-dendritic liquid (continuous films versus isolated pockets) and the primary dendrite arm spacing (PDAS) both determine whether residual liquid can feed and heal incipient cracks. These microstructural features are in turn governed by the local thermal conditions at the solidification front i.e., the thermal gradient (G), solidification velocity (V_s), and crystallographic misorientation angle (θ_R).

The complex interplay between laser beam parameters, thermal conditions and alloy microsegregation during LBW significantly influences the resulting solidification patterns and, consequently, the mechanical properties of the welded joint [2–4]. Recent advances in computational modelling and experimental techniques have paved a way for a more comprehensive understanding of these intricate processes [5,6]. The phase-field (PF) method has gained considerable attention in recent

* Corresponding author at: Institute of Applied Materials (IAM-MMS), Karlsruhe Institute of Technology, Kaiserstrasse 12, Karlsruhe, 76131, Baden-Württemberg, Germany.
Email address: Muhammad.umar@partner.kit.edu (M. Umar).

https://doi.org/10.1016/j.matdes.2026.116332
Received 20 February 2026; Received in revised form 9 May 2026; Accepted 1 June 2026
Available online 3 June 2026

years for its ability to simulate microstructural evolution during solidification processes, including those encountered in LBW [7,8]. This approach allows for the reliable prediction of phase transformations under various thermal conditions and consequently grain structure formation. Local variations in magnitude and direction of thermal gradient (G), solidification velocity (V_s), and melt pool dynamics lead to the formation of various complex solidification structures [9,10]. Dendritic structures growing from opposite fusion surfaces coinciding near the centerline of the weld seam contribute towards the SC probabilities [11].

PF simulations coupled with experimental validation, have provided valuable insights into establishment of the relationship between process parameters and final weld microstructure [12,13]. For instance, Phase-field Algorithms for Computational Engineering (PACE3D) provides a high-performance computational backbone for welding and solidification simulation by enabling large-scale 3D phase-field simulations of microstructure evolution on structured grids [14]. Its optimized stencil-based numerics exploit SSE/AVX vectorization, multidimensional buffering of gradients and fluxes, and cell classification to skip bulk regions, which is crucial for resolving dendritic structures and mushy-zone dynamics at realistic resolutions and domain sizes [15]. The code supports 2D and 3D multiphysics configurations allowing for tailoring computational cost to the specific thermo-chemical coupling in solidification studies. MPI-based 3D domain decomposition with dynamic plane-shifting load balancing to nearly 100,000 cores makes it suitable for HPC campaigns on industrially relevant high speed LBW processes with nano-scale spatial resolution. Within this scalable framework, a broad library of phase-field modules—especially Allen–Cahn, Cahn–Hilliard and advanced Grand-potential formalism-based models dedicated to solidification—have been benchmarked and reported to capture the physics quite well [16–18]. However, there still exists a lack of understanding at sub-micron scale for a comprehensive correlation of local thermal conditions with morphology and microsegregation at various locations in 3D mushy zone especially near the centerline.

Dendritic crystals grow from an unstable solidification front advancing into liquid under specific G and V_s, where the crystallographic orientation strongly influences growth directions due to interfacial energy anisotropy linked to the cubic lattice structure, with preferred growth along the ⟨100⟩. However, competition arises between the imposed thermal gradient direction and the preferred crystalline growth orientation, governed by the misorientation angle (θ_R) between them, as reported in various experimental observations [19–21]. This misorientation leads to diverse dendrite morphologies, including tilted dendrites, seaweed-like patterns, or disordered growth, contrasting with symmetrical dendrites seen under isotropic or low anisotropy conditions [22,23]. Traditional "normal-growth rule" models often neglect crystallographic orientation effects. Understanding and quantifying these misorientation-driven morphological transitions at high velocities remain underexplored but are essential for controlling microstructure evolution. Although there exist simulation studies at various discrete thermal conditions and resulting microstructures, a holistic picture of solidification microstructure of the whole weld pool boundary formed during LBW is still missing.

When experimental data at the millimeter scale are used as input for nanoscale PF simulations, challenges related to data compatibility, handling, and analysis inevitably arise due to the vast difference in spatial resolution and data input/output conditions. This also enhances the probability of human error in further processing experimental data points and individual calculations making the process inefficient [24]. Therefore, Research Data Management (RDM) concept has gained significant attention in recent years due to its crucial role in maintaining research quality and reliability, fostering collaboration among scientists, and accelerating the impact of scientific discoveries [25]. Consequently, the automation of numerical simulation activities is becoming increasingly essential in modern research. This need arises from the necessity to efficiently process diverse experimentally generated data formats as simulation inputs [26,27]. Additionally, robust systems are required to handle, store, and manage the large datasets while complying with the FAIR (Findable, Accessible, Interoperable, and Reusable) principle to ensure availability, completeness, and reproducibility of the research data [28]. FAIR-compliant workflows such as those in Kadi4Mat [29,30] improve data accessibility which is essential to strike a balance between generality and user-friendliness in workflow design for researchers [31–33]. However, there still exists a lack of studies on development of automated workflows for simulations streamlining the process of parameter optimization and sensitivity analysis, allowing for more efficient exploration of the vast parameter space in LBW.

This study aims to bridge the gap between experimental observations and computational predictions by employing an automated PF study to investigate the influence of local thermal conditions on solidification behavior in LBW. To enhance the efficiency and reproducibility of our computational studies an automated workflow for simulation activities is used along with the numerical simulation scheme, mathematical model and experimental methodology as detailed in Section 2. The central objective of this study is therefore to establish, through an automated physics-based simulation framework validated against experiments, a quantitative map relating local (G, V_s, θ_R) conditions to solidification microstructure in LBW of EN 1.4301 austenitic stainless steel. The detailed 2D and 3D results are presented in Section 3 separately. These findings inform the practical design space for defect avoidance, as discussed in Sections 4 and 5.

2. Methods

The methodology of this study is structured around three primary tasks, each integral to the holistic approach for understanding the influence of local thermal conditions on solidification patterns in LBW. The first task involves carrying out the LBW experiments and the calculation of 3D weld pool isotherms using CFD simulation with the ANSYS Fluent software as explained in Sections 2.1 and 2.2, respectively. ANSYS Fluent, a robust computational tool, is employed to simulate the thermal profiles within the weld pool during the LBW process. These simulations are meticulously validated against experimental observations to ensure accuracy. High-speed imaging and thermal cameras are used to capture real-time data on the weld pool dynamics, which serve as a benchmark for validating the CFD simulation results. The alignment between the simulated and experimental isotherms confirms the reliability of the CFD-model in predicting the thermal conditions within the weld pool.

2.1. Experimental setup

The welding experiments were conducted on TruDisk 16,002 disk laser system, having a maximum output power of 16 kW, a beam parameter product of 8 mm x mrad and operating at a wavelength of 1030 nm. As a base material austenitic steel plates EN 1.4301 (X5CrNi18-10) having a thickness of 1 mm have been used. The welding parameters were as follows: laser power of 1 kW, welding speed of 1.2 m/min or 20 mm/s, and a focal position of + 3 mm. Argon with a flow rate of 20 l/min was used as a shielding gas. The thermal cycles were measured by means of two type-K thermocouples (TC) positioned in the middle part of the sample at the distances of 2.1 mm and 3.2 mm to the symmetry plane or centerline of the weld joint respectively as shown in Fig. 1(A). Fig. 1(B) shows the cooling curves plotted with the help of data collected from both the TCs to obtain information about the G involved at an initial stage of solidification.

Two metallographic surfaces are chosen at the upper (S1) and at the middle (S2) cross-section of the weld joint to reveal the variations in the morphology and the chemical segregation of the alloying elements as depicted in Fig. 2. The surfaces S1 and S2 correspond to the circles with radii a1 = 0.1 mm and a2 = 0.05 mm of the laser beam, respectively. These surfaces are described later with greater detail and with multiple magnifications in Sections 3.1.5 and 3.1.6. They are prepared by grinding them with a sand paper with very fine particles down to 1200 grit size. Afterwards the surfaces are polished with diamond suspension with 6 μm, 3 μm and 1 μm grain size as well as 1/4 μm oxide

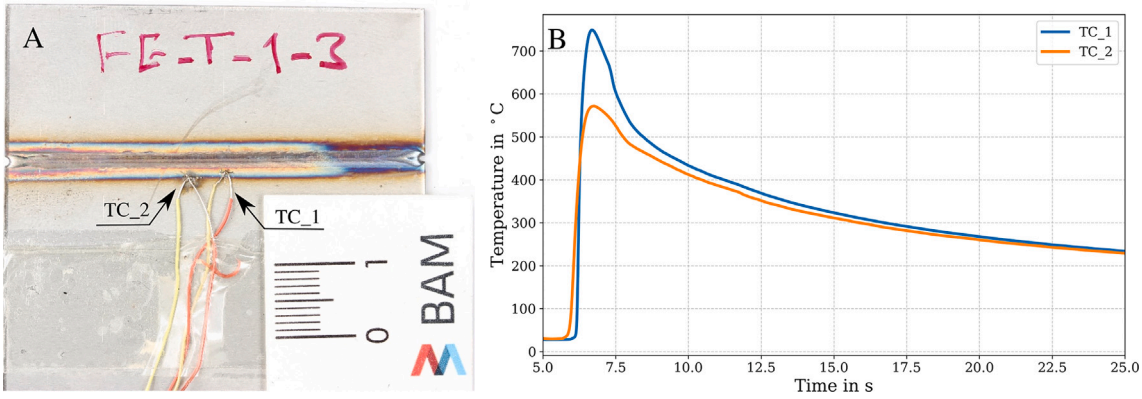

Fig. 1. Experimental setup during LBW with thermocouples TC_1 and TC_2 positioned at the distances of 2.1 mm and 3.2 mm to the symmetry plane through centerline of the weld joint respectively (A). Corresponding cooling curves obtained from these thermocouples (B).

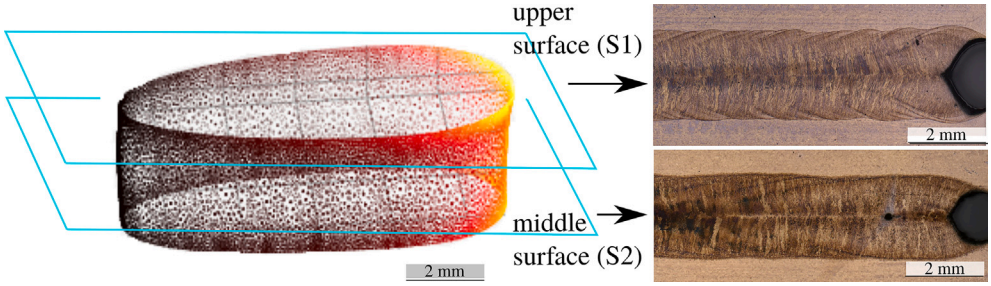

Fig. 2. Weld pool geometry representing liquidus isotherm obtained from ANSYS-based CFD simulation with upper (S1) and middle (S2) surfaces recorded after metallographic preparation.

particle suspension. At the last stage of sample preparation, the polished surfaces are etched with Lichtenegger and Bloech I etchant. The local concentration of alloying elements were measured by means of an electron beam microprobe analyser JEOL JXA-8900 RL.

2.2. CFD simulations

A commercial code ANSYS Fluent is used to establish a simplified Computational Fluid Dynamics (CFD) model of LBW process. The following assumptions/conditions have been adopted:

- Steady-state set of conservation equations for mass, momentum and energy was solved numerically in Euler frame of reference linked to the unmoved laser beam.
- Computational domain in Fig. 3 represents a rectangular block with the size 24 mm by 9.8 mm by 1 mm and has a planar symmetry with respect to one of its side surfaces corresponding to the middle plane of the work-piece (along the welding direction); i.e., only a half of the physical domain has been considered due to the mentioned symmetry.
- The keyhole surface has a form of an axially symmetric cone with a symmetry axis parallel to the beam propagation direction. The Dirichlet boundary condition corresponding to constant temperature (evaporation point) was adopted for this surface; at the same time slip boundary condition for the velocity field was considered at this surface.
- Thermo-capillary force driven convection (Marangoni effect) has been taken into account on the upper and the lower (free) surfaces in the liquid phase as a shear force boundary condition acting on the corresponding surfaces.

More details on applied CFD model can be found in one of the previous publications [34]. This model was used to reconstruct 3D simulation of fluid flow and the temperature distribution near solidification

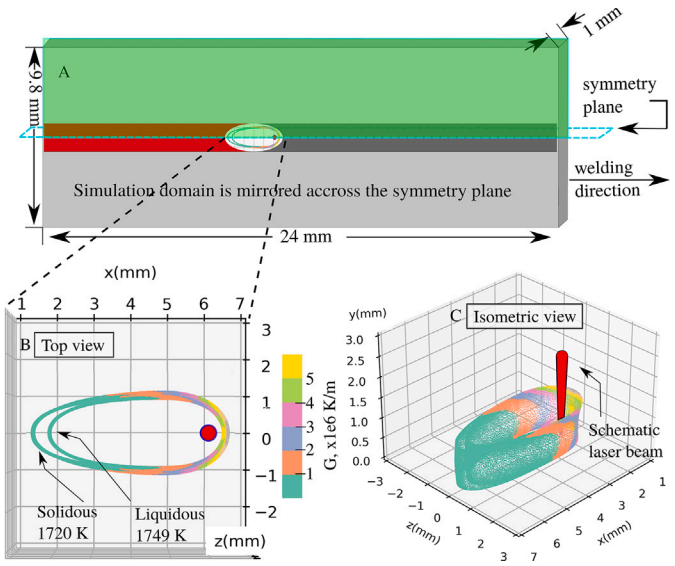

Fig. 3. Computational domain considered for CFD simulations using ANSYS (A). Top view of the isothermal weld pool surfaces obtained as a result of CFD simulation (B) and isometric view (C) at 1720 K and 1749 K.

front. The CFD model is calibrated against the thermocouple measurements described in Section 2.1: the laser absorption coefficient and Marangoni coefficient are iteratively adjusted until the simulated thermal cycles at the TC_1 and TC_2 coordinates match the measured peak temperatures and cooling rates shown in Fig. 1(B). This experimental anchoring ensures that the simulated macroscale temperature field is physically representative within the accessible spatial domain (> 2 mm from the centerline).

Based on the results of the simulations, a dataset containing the coordinates of the isothermal surface corresponding to the liquidus temperature (1749 K) of the EN 1.4301 steel as well as the thermal gradients at nodal points of this surface has been exported as shown in Fig. 3. The local thermal gradient magnitude at any nodal point on the liquidus isotherm is computed directly from the CFD temperature field as:

$$G = |\nabla T| = \sqrt{\left(\frac{\partial T}{\partial x}\right)^2 + \left(\frac{\partial T}{\partial y}\right)^2 + \left(\frac{\partial T}{\partial z}\right)^2}, \tag{1}$$

where the partial derivatives are evaluated at each nodal point of the isotherm surface. The direction of ∇T defines the local heat-flow direction (growth direction of the dendrites), while its magnitude G is used as direct input to the phase-field simulations. The reliability of these CFD-extracted G values is validated indirectly through two checks: (i) matching the predicted liquidus isotherm shape against metallographic cross-sections (Fig. 2), and (ii) the quantitative PDAS agreement at both metallographic surfaces S1 and S2, as discussed in Sections 3.1.5 and 3.2.1.

Macroscopic CFD simulation results provide the V_s direction and thermal gradient along the solidification front which are used as inputs for microscopic PF simulations. The curvature of the isothermal surface at various points is used to get the surface normal to be used as direction of the V_s; refer to Fig. 3(B). Similarly, the corresponding value of the thermal gradient (G) is picked from the same points at the isothermal surface. The points shown with the greenish color as evident from the Fig. 3(C), correspond to the G values less than 1000 K/mm, which in turn are the most interesting values for producing the subsequent solidification microstructure. The higher G values do not let the metal to solidify until the beam passes further and the G drops further below threshold value of 1000 K/mm. The same is true for the current PF simulation study shown with initial 2D simulation detailed in Section 3.1.3. Half of data for producing isothermal surface in Fig. 3 is generated using CFD simulations while the other half is mirrored for the sake of completeness. This pre-processing step of reading the isotherms from the CFD model, mirroring them, calculating the surface normal corresponding to the local curvature, V_s direction and reading G values at points of interest is automatically done using the pre-processing workflow explained in Section 2.4.

2.3. Phase-field model and simulation setup

The second task involves performing PF simulations in both 2D and 3D to investigate the effect of local thermochemical conditions on solidification patterns. For this purpose, a thermodynamically consistent PF approach, built upon a grand potential functional and an Allen–Cahn-type variational formulation, is employed for simulating dendritic solidification patterns in quaternary alloy (Fe-C-Cr-Ni) system. The multi-component multiphase-field model uses multiple order parameters, each representing the local phase fraction for one of the available phases involved in the dendritic solidification. This model including grand-potential-based free energy functional, description of interfacial and bulk contributions and further dependent terms are described in our previous work [16]. Therefore, for the sake of brevity, only governing equation along with necessary optimization employed specifically in this work are explained. The time-dependent evolution behavior of the N phase-fields (ϕ_α) corresponding to $\alpha =$ δ-Fe and Liquid phases, is described by governing equation ensuring consistency with underlying thermodynamic description of the alloy, reading as:

$$\tau\epsilon\frac{\partial\phi_\alpha}{\partial t} = \underbrace{-\epsilon\left(\frac{\partial a(\boldsymbol{\phi},\nabla\boldsymbol{\phi})}{\partial\phi_\alpha} - \nabla\cdot\frac{\partial a(\boldsymbol{\phi},\nabla\boldsymbol{\phi})}{\partial\nabla\phi_\alpha}\right) - \frac{1}{\epsilon}\frac{\partial\omega(\boldsymbol{\phi})}{\partial\phi_\alpha} - \frac{\partial\psi(\boldsymbol{\phi},\boldsymbol{\mu},T)}{\partial\phi_\alpha}}_{:=rhs_\alpha} \underbrace{-\frac{1}{N}\sum_{\beta=1}^{N}(rhs_\beta)}_{:=langrangeMultiplier}. \tag{2}$$

To account for the interplay of different timescales in the evolution equations, a relaxation parameter τ is incorporated to mediate their coupling. The interfacial width is determined by the parameter ϵ, while the structure of the interface is governed by both the gradient energy density $a(\boldsymbol{\phi},\nabla\boldsymbol{\phi})$ and an obstacle potential $\omega(\boldsymbol{\phi})$, reflecting contributions from interface energies as well as potential-induced constraints. $\psi(\boldsymbol{\phi},\boldsymbol{\mu},T)$ is a vector containing individual grand-potentials of the phases. The gradient energy term described as:

$$a(\boldsymbol{\phi},\nabla\boldsymbol{\phi}) = \sum_{\alpha,\beta=1}^{N}\gamma_{\alpha\beta}\left[a_c(\boldsymbol{q}_{\alpha\beta})\right]^2\left|\boldsymbol{q}_{\alpha\beta}\right|^2, \tag{3}$$

which includes the interface energy per unit area of the α/β interface, $\gamma_{\alpha\beta}$ and a function $a_c(\boldsymbol{q}_{\alpha\beta})$ describing anisotropy in the interface energy. This is treated using cubic anisotropic assumptions [35] given as:

$$a_c(\mathbf{q}_{\alpha\beta}) = 1 - \delta_{\alpha\beta}\left(3 - 4\frac{|q_{\alpha\beta}|_4^4}{|q_{\alpha\beta}|^4}\right). \tag{4}$$

The generalized gradient normal vector is given as:

$$\boldsymbol{q}_{\alpha\beta} = \phi_\beta\nabla\phi_\alpha - \phi_\alpha\nabla\phi_\beta. \tag{5}$$

For anisotropic interfaces with cubic four-fold symmetry, the anisotropy function takes the form,

$$a_c(\boldsymbol{q}_{\alpha\beta}) = 1 - \delta_{\alpha\beta}\left(3 - 4\frac{|\boldsymbol{q}_{\alpha\beta}|_4^4}{|\boldsymbol{q}_{\alpha\beta}|^4}\right), \tag{6}$$

where,

$$|\boldsymbol{q}_{\alpha\beta}|_4^4 = \sum_{i=1}^{3}\left(q_{\alpha\beta,i}\right)^4, \quad |\boldsymbol{q}_{\alpha\beta}|^4 = \left(\sum_{i=1}^{3}\left(q_{\alpha\beta,i}\right)^2\right)^2, \tag{7}$$

with $i = x, y, z$ denoting Cartesian components, and $\delta_{\alpha\beta}$ is the anisotropy strength for the interface. To account for the local phase misorientation angle $\theta_{\alpha\beta}$ between two adjacent phases, the gradient vector is rotated by the orthogonal rotation matrix $\boldsymbol{R}_{\alpha\beta}(\theta_{\alpha\beta})$,

$$\boldsymbol{q}_{\alpha\beta}^{rot} = \boldsymbol{R}_{\alpha\beta}^T\cdot\boldsymbol{q}_{\alpha\beta}, \tag{8}$$

where $\boldsymbol{R}_{\alpha\beta}$ is given by:

$$\boldsymbol{R}_{\alpha\beta} = \begin{bmatrix} R_{11} & R_{12} & R_{13} \\ R_{21} & R_{22} & R_{23} \\ R_{31} & R_{32} & R_{33} \end{bmatrix}, \tag{9}$$

with orthogonality conditions and parameters defining rotation axis and angle. For instance, if the rotation is about any of the three fundamental axes i.e., x, y, z, it is simply represented as:

$$\boldsymbol{R}_{\alpha\beta}(\theta_{\alpha\beta}), x = \begin{bmatrix} 1 & 0 & 0 \\ 0 & \cos\theta_{\alpha\beta} & -\sin\theta_{\alpha\beta} \\ 0 & \sin\theta_{\alpha\beta} & \cos\theta_{\alpha\beta} \end{bmatrix}, \tag{10}$$

$$\boldsymbol{R}_{\alpha\beta}(\theta_{\alpha\beta}), y = \begin{bmatrix} \cos\theta_{\alpha\beta} & 0 & \sin\theta_{\alpha\beta} \\ 0 & 1 & 0 \\ -\sin\theta_{\alpha\beta} & 0 & \cos\theta_{\alpha\beta} \end{bmatrix}, \tag{11}$$

$$\boldsymbol{R}_{\alpha\beta}(\theta_{\alpha\beta}), z = \begin{bmatrix} \cos\theta_{\alpha\beta} & -\sin\theta_{\alpha\beta} & 0 \\ \sin\theta_{\alpha\beta} & \cos\theta_{\alpha\beta} & 0 \\ 0 & 0 & 1 \end{bmatrix}. \tag{12}$$

Replacing $\boldsymbol{q}_{\alpha\beta}$ with $\boldsymbol{q}^{rot}_{\alpha\beta}$ in Eq. (6) yields the rotated anisotropy function

$$a_c(\boldsymbol{q}^{rot}_{\alpha\beta}(\theta_{\alpha\beta})) = 1 - \delta_{\alpha\beta}\left(3 - 4\frac{\sum_{i=1}^{3}\left(q^{rot}_{\alpha\beta,i}\right)^4}{\left(\sum_{i=1}^{3}\left(q^{rot}_{\alpha\beta,i}\right)^2\right)^2}\right), \tag{13}$$

which fully incorporates the effect of bicrystal misorientation on the interfacial anisotropy and microstructural evolution in 3D.

The driving force for solidification is taken from the difference in the grand potential, $\Psi_\alpha(T, \boldsymbol{\mu}, \Phi)$. CALPHAD-based thermodynamic description provided by [36] is used to parabolically fit the Gibbs energy functions for all the involved phases whose details are given elsewhere [16]. A Lagrange multiplier in Eq. (2) enforces the conservation constraint on the PF variables, such that their total sum at any point in domain always stays zero, ensuring physically consistent kinetics throughout the simulation.

To maintain mass conservation within the simulation process, a time-dependent formulation for the chemical potentials is implemented and directly coupled to the PF evolution equation. The chemical potential vector $\boldsymbol{\mu}$ includes an individual parameter μ_i assigned to chemical species (where i = Fe,C,Cr,Ni), and the dynamic changes in these potentials are determined based on the mass conservation requirements of the four chemical concentrations in the present study. This coupling ensures the appropriate transport and redistribution of each species.

$$\frac{\partial \boldsymbol{\mu}}{\partial t} = \left[\sum_{\alpha=1}^{N} h_\alpha(\boldsymbol{\phi})\left(\frac{\partial c_\alpha(T,\boldsymbol{\mu})}{\partial \mu}\right)\right]^{-1}\left(\nabla\cdot\left(\mathbf{M}(T,\boldsymbol{\mu},\boldsymbol{\phi})\nabla\boldsymbol{\mu} - \mathbf{J}_{at}(T,\boldsymbol{\mu},\boldsymbol{\phi})\right)\right.$$
$$\left. - \sum_{\alpha=1}^{N}\mathbf{c}_\alpha(T,\boldsymbol{\mu})\frac{\partial h_\alpha(\boldsymbol{\phi})}{\partial t} - \sum_{\alpha=1}^{N} h_\alpha(\boldsymbol{\phi})\left(\frac{\partial c_\alpha(T,\boldsymbol{\mu})}{\partial T}\right)\frac{\partial T}{\partial t}\right). \tag{14}$$

In this context, the vectors $c_\alpha(T, \boldsymbol{\mu})$ represent the concentrations of alloying elements such as Fe, C, Cr and Ni within the considered phase α. The mobility term $\mathbf{M}(T, \boldsymbol{\mu}, \boldsymbol{\phi})$ comprises of the diffusion coefficient matrix D^α_{ij} for all participating phases, while the function $h(\boldsymbol{\phi}_\alpha) = \boldsymbol{\phi}^2_\alpha(3 - 2\boldsymbol{\phi}_\alpha)$ is constructed to smoothly interpolate phase properties between the distinct phases. Additionally, the anti-trapping flux $\mathbf{J}_{at}(T, \boldsymbol{\mu}, \boldsymbol{\phi})$ is typically implemented in PF simulations to mitigate spurious solute trapping that arises when the numerical interface thickness ϵ greatly exceeds the physical metallic interface thickness (0.1–0.5 nm).

Another important discussion in the literature is on the validity of equilibrium assumptions in PF models for LBW-associated local thermal conditions. PF models have been developed for multiple phase transition processes like casting, welding, and additive manufacturing. Some of them have process-related high V_s or growth rate (R), where local thermal equilibrium conditions are violated and a modified non-equilibrium formulation is required as presented by Segawa et al. [37]. Local equilibrium at the interface is assumed for the process currently studied where $R < 20$ mm s^{-1}. This is supported by Aziz's Continuous Growth Model (CGM) [38] and subsequent PF studies [39] which show significant deviation of interface velocity dependent partitioning coefficient $(k(v))$ from equilibrium partitioning coefficient (k_0) only for $R > 300$ mm s^{-1}. Kavousi et al. [40] reported after a comprehensive comparative PF study that simulation results are very close to the analytical results for $R < 200$ mm s^{-1} with quasi-equilibrium solidification assumptions. It also shows that when the V_s increases, the PF results deviate from the analytical predictions, with the maximum difference between (k_0) and $(k(v))$ of 14% at $R = 600$ mm s^{-1}, thus making the equilibrium assumption invalid. The remaining non-equilibrium kinetic effects in this study are captured through: (i) the dynamic chemical potential formulation (Eq. (14)), which governs solute redistribution at the moving interface under the local-equilibrium assumption; (ii) the relaxation coefficient $\tau_{S/L} = 4\times10^8$ J·s/m^4, which ensures the interface velocity is consistent with the local thermodynamic driving force; and (iii) the frozen temperature approximation (Eq. (15)), which imposes a kinetic constraint on the temperature field evolution consistent with the prescribed G and V_s.

The progression of temperature in the system is characterized using a dynamic analytic framework, which captures its evolution through a moving reference solution, known as frozen temperature approximation. This method allows for a precise mathematical representation of how temperature changes as a function of position and time, reflecting the influence of a continuously relocating heat source or front. By applying this moving analytic approach, the temporal and spatial development of temperature can be systematically described as:

$$\frac{\partial T}{\partial t} = \frac{\partial}{\partial t}\left(T_0 + G\left(x - V_G t\right)\right) = -GV_G. \tag{15}$$

Initial temperature $T_0 = T_s - \Delta T$ is set at the left edge of the domain and is distributed to the right edge according to the thermal gradient G. The movement of the this thermal distribution is controlled using thermal gradient velocity V_G in the direction of growth of solidification i.e., x-direction. T_s and ΔT are solidification temperature and thermal undercooling, respectively.

2.3.1. Computation and physical parameters

All simulations are carried out using parameters as detailed in Table 1, or specifically defined where used otherwise.

The solid–liquid interfacial energy $\gamma_{S/L} = 0.25$ J/m^2 (2D simulations) is adopted from Yang et al. [41], who reported the value for Fe-based alloys using a multiphase-field model structurally identical to the PACE3D formulation employed here. Direct experimental measurements of $\gamma_{S/L}$ for the quaternary Fe–Cr–Ni–C system at LBW-relevant temperatures (> 1720 K) are not available in the published literature; the values used represent the best available estimates for the Fe-based alloy class.

The cubic anisotropy strength $\delta_{\alpha\beta} = 0.06$ is a widely adopted value in phase-field models for BCC and FCC metals, consistent with experimental estimates of solid–liquid interface anisotropy in metallic systems. This value was chosen to reproduce the experimentally observed dendritic (rather than purely cellular) morphology in the intermediate G range studied, providing an implicit morphological calibration.

The simulated dendrite tip radius scales as $R_{\text{tip}} \propto \gamma^{0.42}_{S/L}$ (Fig. 4(a)), in close agreement with the theoretical exponent of 0.5 predicted by marginal stability theory [42,43], confirming that the model correctly captures the capillary-dominated morphological selection. A ±20% variation in $\gamma_{S/L}$ around the calibrated value therefore translates to approximately ±10% variation in the predicted PDAS—consistent with the observed 12 % PDAS deviation at S1 and < 4% deviation at S2. This quantitative PDAS agreement at both metallographic cross-sections

Table 1
Physical parameters used for various simulations.

Simulation Parameters for 2D and 3D simulations	
Parameter	*Value*
Δx, Δy, Δz	2×10^{-8} m
Nx, Ny	10.08 µm, 10 µm
Nx, Ny, Nz for 3D	12.8 µm, 12.8 µm, 19.2 µm
Δt	4×10^{-8} s
Δt for 3D	2×10^{-8} s
Interface thickness parameter (ϵ)	4×10^{-8} m
Initial temperature (T_0)	1738 K
Thermal gradient (G)	100 K/mm - 900 K/mm
Surface Energy ($\gamma_{S/L}$)	0.25 J/m^2 [41]
Surface Energy for 3D ($\gamma_{S/L}$)	0.18 J/m^2
Relaxation Coefficient ($\tau_{S/L}$)	4×10^8 J s/m^4
Solid diffusion coefficient (D^α_{ii})	1×10^{-12} m^2/s
Liquid diffusion coefficient (D^α_{ii})	1×10^{-9} m^2/s
Concentration noise amplitude, (ξ_i)	0.00005
Cubic anisotropy strength, ($\zeta_{\alpha\beta}$)	0.06

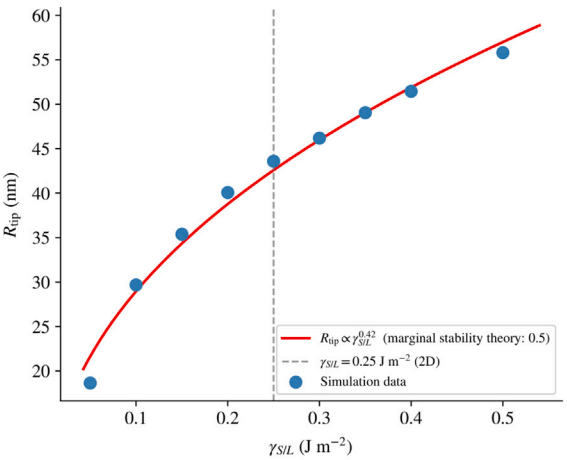

(a) Mean dendrite tip radius R_{tip} as a function of solid–liquid interfacial energy $\gamma_{S/L}$, from 9 phase-field simulations at fixed thermal conditions ($G \approx 300$ K/mm, $V_s = 5$ mm/s). The power-law fit $R_{tip} \propto \gamma_{S/L}^{0.42}$ is in close agreement with the theoretical exponent of 0.5 from marginal stability theory. Dashed vertical line marks the calibrated value of interfacial energy used in the 2D ($\gamma_{S/L} = 0.25$ J/m^2) and 3D ($\gamma_{S/L} = 0.18$ J/m^2) simulations.

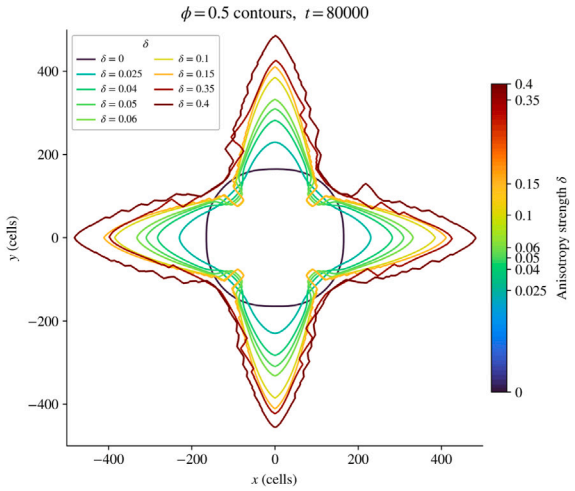

(b) $\phi = 0.5$ contour lines from 2D phase-field simulations of a single equiaxial seed growing under varying anisotropy strength δ (colour-coded). Low δ gives a nearly circular interface (isotropic growth); increasing δ progressively introduces cubic four-fold symmetry. The value $\delta_{\alpha\beta} = 0.06$ used in this study provides a moderate cubic character consistent with the experimentally observed dendritic morphology.

Fig. 4. Calibration of interfacial parameters. (a) Dendrite tip radius scaling with interfacial energy $\gamma_{S/L}$. (b) Phase-field contours for varying anisotropy strength δ.

under independent thermal conditions constitutes a strong implicit validation of the combined parameter set: such agreement would not be achieved if either $\gamma_{S/L}$ or $\delta_{\alpha\beta}$ were substantially in error. ≈18 hours were taken by each 2D simulation till steady state growth conditions. A concept of the moving window approach is utilized in this work. The moving window strategy in solidification simulations is aimed at reducing computational cost by restricting the computation during solution of equations to a smaller, dynamically shifting region of interest—here the solidification front within a large domain. This technique is especially beneficial for thermochemically coupled simulations, where computational efficiency and accuracy are critical [44,45]. This method ensures precise capturing of crucial phenomena such as dendrite growth and microsegregation development inside the defined window without sacrificing the representativeness of the whole volume. Boundary conditions for the window are continuously updated to reflect the state of the surrounding larger domain. To avoid boundary artifacts, the window is designed to include at least 5 × diffusion lengths of liquid ahead of the solidification front in the growth direction [46]. The 3D simulations were performed under the same boundary conditions and with the same hardware resources, with the exception of the number of cores, which in this case is 1200. A 3D domain with 25.6 × 25.6 × 19.2 μm dimensions was simulated with 393.216 million cells for 3 days, with computational cost compared to the direct CALPHAD coupling methods [47].

2.4. Automation workflow

The PACE3D solver is integrated into a workflow scheme of Kadi4Mat framework to streamline and automate the simulation process. Through this automated workflow, systematic parameter studies and sensitivity analyses can be conducted efficiently, substantially reducing the manual effort typically required for configuring and running large numbers of simulations. Therein, the PF method is employed to simulate the microstructural evolution during solidification under varying thermal conditions. The automation provided by Kadi4Mat therefore plays a central role in guaranteeing reproducibility, scalability, and efficiency when performing extensive simulation studies. The approach employs a sequential, one-way coupling from macroscale CFD to microscale PF, mediated by the Kadi4Mat workflow. The key technical features are as follows:

2.4.1. Main-processing module of the workflow

Macroscale CFD simulations with ANSYS Fluent on $24 \times 9.8 \times 1$ mm^3 domain is performed to solve the steady-state conservation equations for mass, momentum, energy, and species transport. Key outputs are the 3D liquidus isotherm surface at multiple temperatures from T = 1749 K – 1679 K, the thermal gradient value $\mathbf{G}$ at nodal points on this surface and the surface normal vector $\hat{\mathbf{n}}$ (defining the local V_s and $\mathbf{G}$ direction). Kadi4Mat scale-bridging module automates the following steps:

(i) *Data retrieval:* The 3D CFD isotherm dataset (coordinates and G values) is automatically downloaded from the Kadi4Mat repository using its API.
(ii) *Sub-domain extraction:* Multiple representative sub-domains are identified along the liquidus isotherm, spanning the full range of G and V_s conditions from the fusion line to the weld centerline. Sub-domain positions are selected programmatically to sample the parameter space uniformly.
(iii) *Local parameter calculation:* For each RVE, the local G is read directly from the CFD nodal data, and the dendrite growth angle i.e., the angle between the isothermal surface normal and the welding direction, is computed by fitting a local least-squares tangent plane to the isothermal surface coordinates.
(iv) *Thermosolutal Gibbs energy generation:* CALPHAD equilibrium concentrations and Gibbs free energy values for the Fe–Cr–Ni–C system are extracted from the thermodynamic database using Thermo-Calc and fitted to parabolic thermosolutal functions (linear or second-order polynomial, selected by minimising mean squared error) for use as thermodynamic driving forces.
(v) *Input file generation and HPC submission:* PF simulation input files are automatically assembled for each sub-domain incorporating local G, V_s, and θ_R, domain dimensions, and thermosolutal parameters. Files are submitted to the HPC cluster with automatically computed optimal domain decomposition settings.

Microscale PACE3D simulations with ~10–60 μm^2 in 2D and 25.6 × 25.6 × 19.2 μm^3 in 3D sub-domains receive the macroscopically extracted G and V_s as boundary conditions via the frozen temperature approximation (Eq. 14). The thermodynamic driving force is supplied by the CALPHAD-fitted Gibbs energy functions. Post-processing (PDAS,

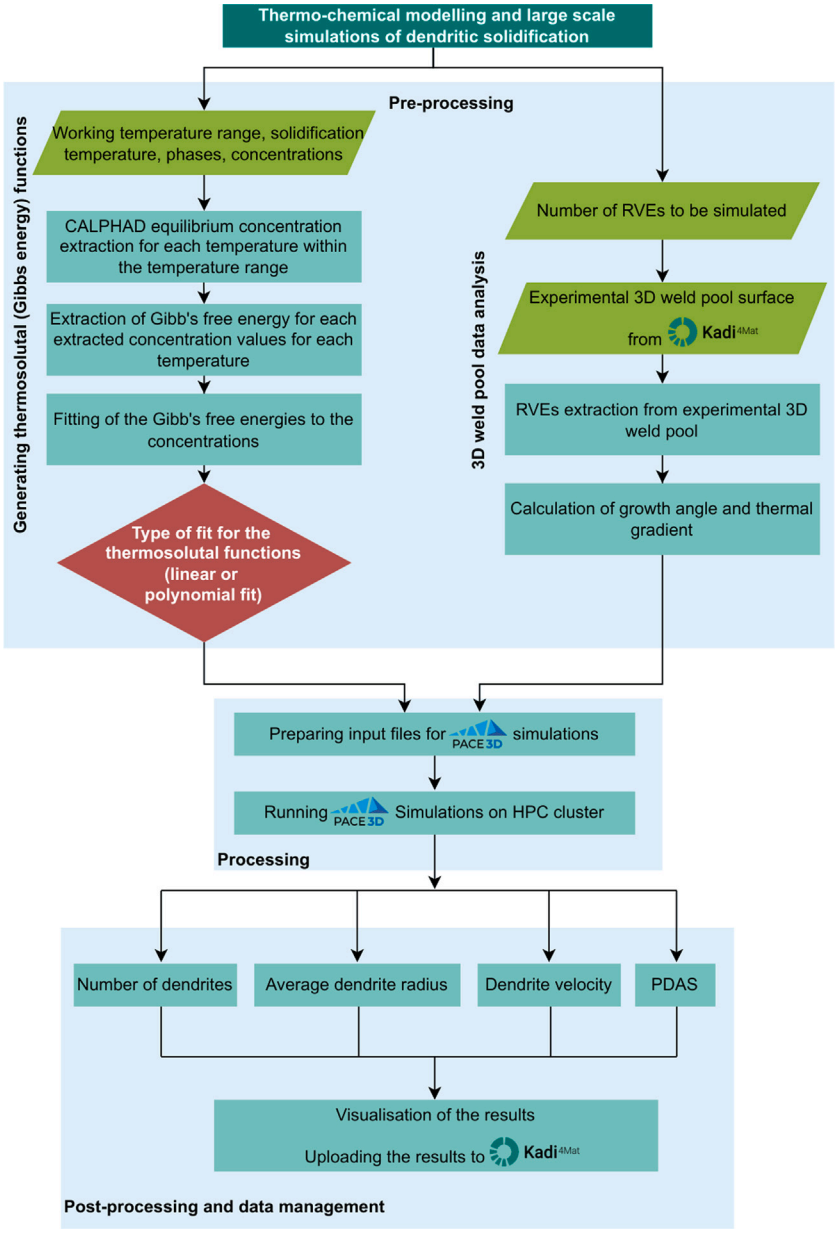

Fig. 5. Kadi4Mat workflow used to carry out pre-, main- and post-processing activities in phase-field simulation studies utilizing the PACE3D simulation environment.

R_{tip}, V_{tip}, dendrite count) is performed automatically upon simulation completion and the results are uploaded to the Kadi4Mat repository.

The Kadi4Mat workflow has managed and executed more than 160 PF simulations in the present study, generated by a parametric grid of 5 values of the thermal gradient G (100–900 K/mm), 8 values of the solidification rate R (0.005–0.04 m/s), and 4 values of the misorientation angle θ_R, with each simulation requiring ~18 hours to reach steady state on 128 compute nodes. Pre-processing tasks that would otherwise be carried out manually have been fully automated. CALPHAD data extraction and thermosolutal Gibbs energy fitting are reduced from ~2 h per alloy–temperature combination to ~5 min, with the workflow automatically evaluating more than 50 candidate parabolic fits per quaternary composition to identify the best least-squares match to the Gibbs energy values. PF input file generation and HPC job submission are reduced from ~30 min to less than 1 min per simulation, corresponding to a cumulative saving of more than 200 hours over the present study. The identification of weld-pool surface coordinates and normal directions from the CFD output, previously a manual step, is now handled by a Python surface-fitting module. All simulation inputs, parameters, and post-processed outputs (PDAS, R_{tip}, V_{tip}, dendrite count) are automatically extracted and uploaded to the Kadi4Mat repository, providing FAIR-compliant data management and eliminating the transcription errors and version conflicts that are non-trivial risks when handling hundreds of large-scale simulation datasets manually.

The present workflow has three main limitations. First, it is restricted to steady-state LBW conditions, where the weld-pool geometry and thermal field remain statistically stationary; extension to transient simulations (e.g., pulsed laser welding or keyhole oscillations) is easily achievable provided the experimental observations are available. Second, the CFD model carries inherent uncertainties in the laser absorption coefficient, Marangoni coefficient, and keyhole surface geometry, calibrated against thermocouple data; formal uncertainty quantification (e.g., Monte Carlo sensitivity analysis) is beyond the scope of this study. Third, the G and V_s values extracted at the liquidus isotherm are treated as locally uniform inputs to each PF sub-domain, justified by scale separation. However, it requires re-evaluation for relatively larger PF sub-domains. A schematic of the workflow is shown in Fig. 5.

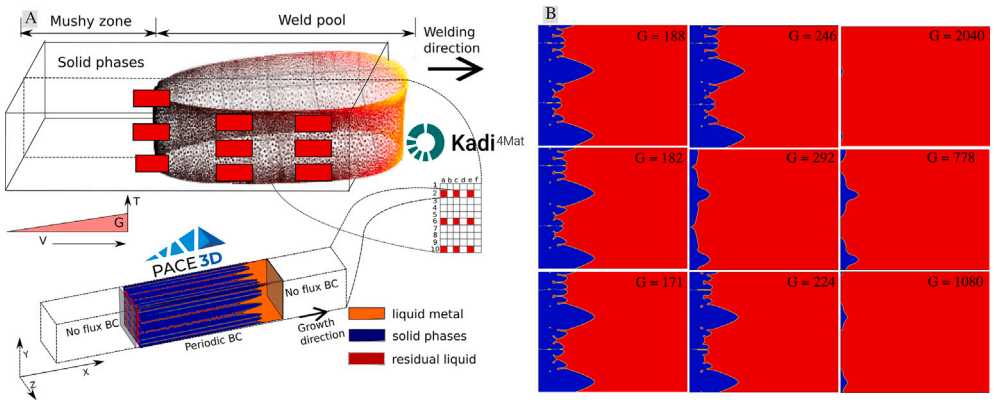

Fig. 6. Schematic representation of automated extraction of simulation sub-domains from solidus surface using the Kadi4Mat workflow (A). Initial results of the automated 2D simulations showing variation in the thermal gradient (G) from 188 K/mm to 2040 K/mm (B).

3. Results

3.1. 2D results

3.1.1. Simulating the whole weld pool

To investigate the influence of local thermal conditions on microstructural patterns during solidification in LBW, the experimental 3D liquidus surface of the weld pool is considered as a basis for simulation study. Performing a single high-resolution PF simulation to capture the entire weld pool's microstructural evolution—for instance, at a spatial resolution of 5 nm—is computationally unfeasible, owing to the immense resource demands and system complexity. Therefore, a schematic division of the full 3D domain into multiple sub-domains is implemented, allowing for individual PF simulations of each sub-domain as illustrated schematically in Fig. 6(A). This approach assigns periodic boundary conditions to the sides in each domain to effectively mimic the continuous nature of the weld pool while remaining computationally feasible. Such segmentation enables thorough and localized analysis without sacrificing the spatial fidelity or continuity needed for accurate weld pool representation.

By running multiple simulations of local domains systematically distributed in the weld pool geometry, the evolution across the full weld pool is evaluated, leveraging parallel computational strategies and representative local thermal gradients and velocities thereof. This methodological framework provides reliable and scalable insights into dendritic pattern formation and microsegregation behavior under realistic LBW conditions. This approach not only bridges the gap between discrete simulation studies and actual welding outcomes but also offers valuable insights into the complex relationship between local thermal conditions and microstructural evolution throughout the mushy zone. Using the established workflow and the multiphase-field solver PACE3D, 2D simulations are performed according to the parameters and computational conditions explained in Section 2.3.1. To holistically simulate the weld pool, 9 different domains on the solidus surface are selected automatically as shown in Fig. 6, using the automated Kadi4Mat workflow. The sub-domains to be simulated are shown with red rectangles schematically on the weld pool surface obtained through CFD simulations shown in Fig. 6(A). Periodic boundary conditions are imposed on the top and bottom boundaries of the two-dimensional domain to simulate an infinitely repeating structure in those directions. At the left and right edges, a no-flux condition is enforced using Neumann boundary conditions, ensuring that there is no material transfer across these boundaries.

Fig. 6(B) presents the initial results corresponding to 9 sub-domains takes at 9 rectangles highlighted in red schematically in Fig. 6(A). During the initial microstructure evolution, it is observed that after specific time (t), certain sub-domains specifically those above G = 778 K/mm exhibit no continuous solidification rather remelting. In contrast, regions below G = 778 K/mm show accelerated microstructure growth. It is evident that the surface areas with G values below approximately 778 K/mm present the most favorable sites for solidification as opposed to higher G values where melting is in progress. Accordingly, in further comprehensive 2D simulation studies, a threshold value of $G < 700$ K/mm is employed to investigate regions suitable for solidification and microstructure evolution.

3.1.2. Parametric study

To have a holistic view of the dependence of dendrite growth rate (R) and G a set of automated simulations are conducted across a parameter space spanning G from 100 to 900 K/mm and V_s or R from 0.005 to 0.04 m/s to systematically quantify how local thermal conditions govern dendritic morphology. For simulations with higher G values the domain must be resolved more i.e., up to ($\Delta x = 5$ nm); therefore anti-trapping being least relevant is ignored in these simulations. Fig. 7(A–C) presents 3D surfaces constructed from simulation results, each capturing distinct microstructural metrics. Fig. 7(A) reveals that (R_{tip}) decreases monotonically with increasing R and increasing G, reflecting the competition between thermal and solutal diffusion lengths that control final morphology. Fig. 7(B) demonstrates that dendrite number density peaks at elevated G combined with R, a regime where constitutional undercooling allows sustenance of multiple competing dendrites. Fig. 7(C) shows PDAS reduces with both increasing R and G, consistent with Ivantsov–Trivedi scaling predictions: finer structures emerge under steeper thermal fields and faster solidification kinetics [48]. Fig. 7(D) contextualizes these quantitative surfaces within the classical solidification diagram, mapping planar → cellular → columnar dendritic → equiaxed dendritic transitions. The current study only takes into account a subset of the figure with only cellular and columnar dendritic morphology highlighted in light green in Fig. 7(D). The simulated microstructural trends align qualitatively with established morphology selection criteria, validating the PF approach.

3.1.3. Influence of misorientation angle (θ_R)

Along with the two processing parameters i.e., G and R, another critical factor that needs investigation is the θ_R. Fig. 8 presents a systematic sequence of frames at advancing time from a single 2D PF simulation highlighting the effect of θ_R and growth competition among dendrites growing at different θ_R (i.e., 0°, 15°, 30°, and 45°) on solidification microstructure under a fixed G. Fig. 8(A–G) corresponds to an increasing simulation time (t) tracing the progression of competitive dendritic growth for distinct grain orientations. θ_R is indicated by the color legend where red color indicates the direction of G which remains constant throughout the domain. Green colored arrows indicate the ⟨100⟩ direction of growing cubic crystal, varying from 0° to 45°. The time series from A to G reveals pronounced sensitivity of θ_R

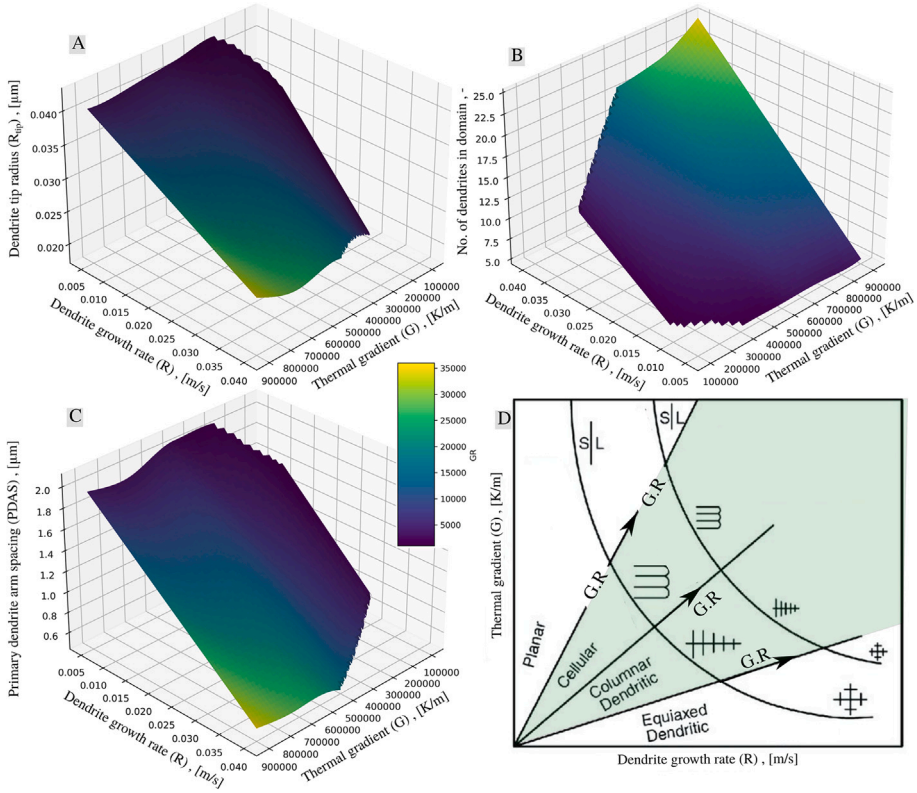

Fig. 7. 3D surfaces from PF simulations showing (R_{tip}) (A), number density of dendrites (B), and PDAS (C) as functions of G (K/m) and R (m/s), with a classical solidification morphology diagram illustrating planar, cellular, columnar dendritic, and equiaxed dendritic regimes [49] (D).

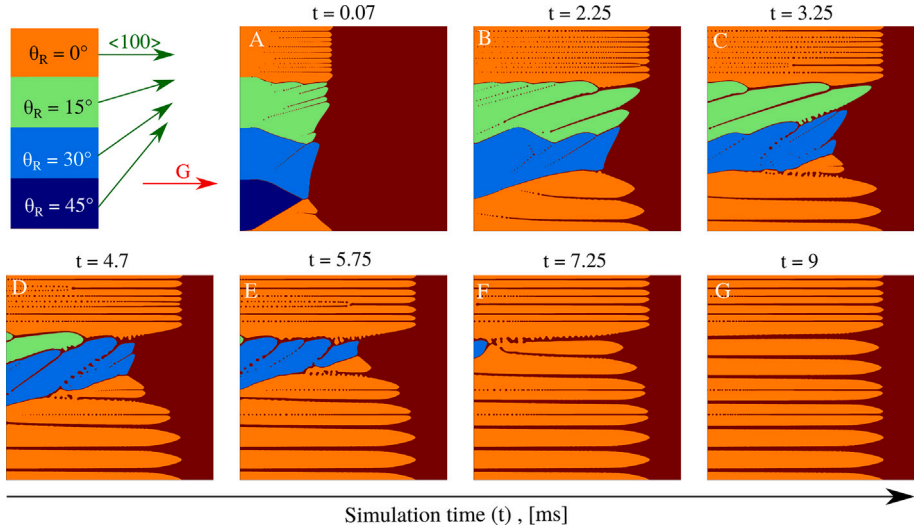

Fig. 8. 2D PF simulation result of dendritic growth, showing the evolution of microstructure as a function of θ_R (A to G), with color denoting grain orientation (0°, 15°, 30°, and 45°) and their mutual competition during growth until dendrite with minimum θ_R survives. (For interpretation of the references to color in this figure legend, the reader is referred to the web version of this article.)

illustrating that cubic crystals with their ⟨100⟩ orientation aligned with the temperature gradient, last longer. It is clear from the first two time instances that maximum $\theta_R = 45°$ vanishes from the competition because the preferred growth direction is not aligned with G. It is evident from Fig. 8(C–F), that misoriented crystals are progressively overgrown by favorably aligned grains, consistent with classical theories of directional solidification [50–52]. This behavior is well captured by the PF formulation's coupling of interface kinetics and orientation-dependent growth rates. It is clear from Fig. 8 that impact of initially present less favorably oriented cubic crystals is minimum on the microstructure obtained at later stage of solidification i.e., near the centerline of the weld seam. Therefore the microstructure will be dominated by θ_R available as the most favorable in the competition.

A comprehensive overview of 2D PF simulation results, highlighting the morphological evolution of dendrites under relevant thermal gradients (100–700 K/mm) and misorientation angles ($\theta_R = 0°, 15°, 30°,$

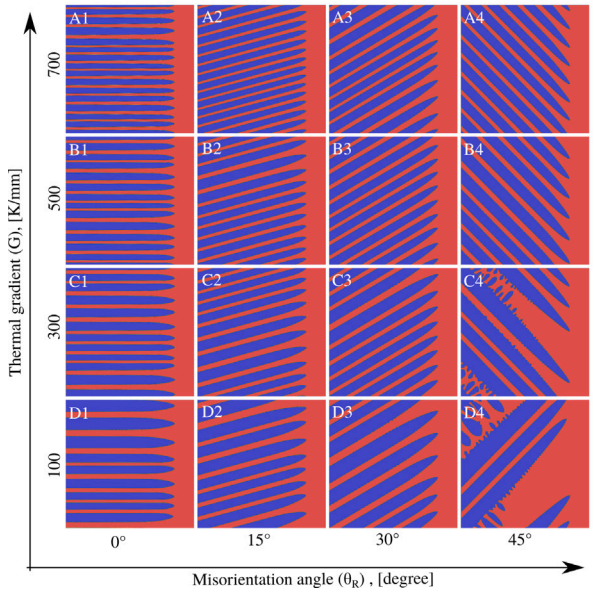

(a) The effect of misorientation angle (θ_R) i.e., 0°, 15°, 30°, and 45° (from left to right-A1 to D4) and thermal gradient i.e., 100 K/mm, 300 K/mm, 500 K/mm, and 700 K/mm (from bottom to top) on the dendritic morphology at V_{tip} of 20 mm/s simulated through the automated Kadi4Mat workflow.

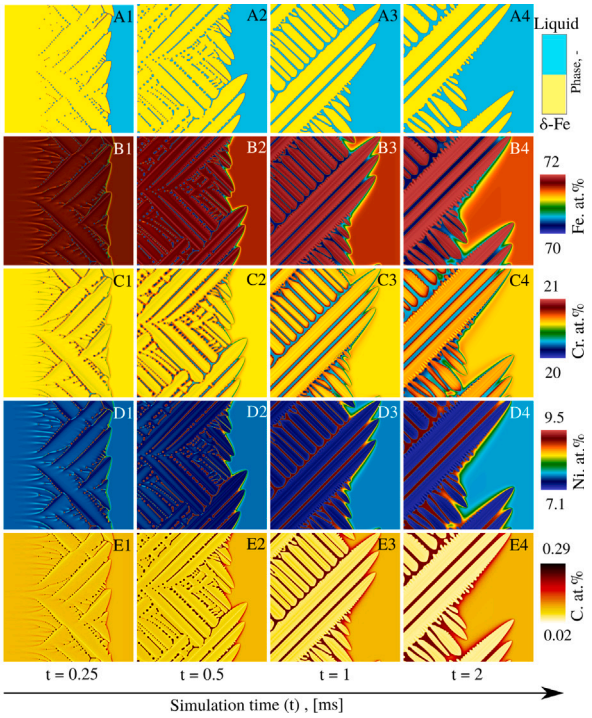

(b) Evolution of the dendritic morphology at solidification front velocity of 20 mm/s and θ_R = 45°, showing the phase field (A1–A4) and the segregation of Fe (B1–B4), Cr (C1–C4), Ni (D1–D4), and C (E1–E4).

Fig. 9. 2D PF simulation results at V_s = 20 mm/s: (a) combined effect of misorientation angle θ_R and thermal gradient G on the dendritic morphology; (b) temporal evolution of the dendritic morphology and solute segregation fields at θ_R = 45°.

and 45°) at a constant V_s of 20 mm/s are shown in Fig. 9(a). Fig. 9(a) presents a set of 2D PF simulation results mapping the evolution of dendritic microstructures during quasi-directional solidification. The blue regions represent solid dendrites, while the red background corresponds to the surrounding liquid phase. These simulations were systematically conducted and managed using the implemented workflow, which streamlined the entire process—from automated pre-processing and execution of the simulations to post-processing and saving the results on kadi4Mat platform, ensuring efficient data reuse and sharing.

From left to right columns 1–4 show the θ_R from 0° to 45° relative to the imposed G values 700 to 100 K/mm as shown in rows A–D. This arrangement enables isolation of the combined influence of θ_R and growth conditions on dendritic pattern selection. A generally decreasing PDAS trend is observed when G is increased from 100 to 700 K/mm for all the θ_R cases. This can also be observed that with an increase in G there exists a gradual increase in number density of dendrites. For instance, for θ_R =0°, for 100, 300, 500, and 700 K/mm there are an increasing number dendrites observed i.e., 9, 11, 13, and 15, respectively. As θ_R increases not only is a shift in growth direction observed but also a clear widening in primary dendrite width is observed accordingly, maintaining their growth defined by θ_R, consistent with classical crystallographic growth selection theory [53]. This effect is particularly prominent at higher orientation angles, with dendrites at 45° showing broader arms and less uniformity compared to the relatively slender dendrites at 0°. For low to moderate θ_R (A1-A3), (B1-B3), (C1-C3), and (D1-D3), the Primary Dendrite Arms (PDAs) remain cellular and exhibit stable morphologies across the entire range. At lower G (lower rows), particularly for larger θ_R (columns 4), the simulations reveal a marked transition from regular, steady-state dendritic growth to complex patterns featuring side-branch formation and pronounced morphological instability. These features are most pronounced in Fig. 9(a) (panels C4 and D4), highlighting the interplay between θ_R and instability thresholds. These different cases of θ_R demonstrate that misorientation alters primary dendrite array alignment, modifies PDAS, induces competitive growth among primary dendrites, and regulates the spatial distribution of secondary dendrites.

Fig. 9(b) presents the evolution of microstructure at different time steps and chemical segregation during dendritic solidification in a quaternary alloy, simulated using a 2D PF approach at a fixed misorientation angle of θ_R = 45°. In Fig. 9(b), panels A1–E4 correspond to increasing solidification time from left to right, with row A showing the phase field and rows B–E showing the concentration fields, capturing stages from initial interface perturbation through the development and coarsening of PDAs and SDAs. Each row (A–E) visualizes a distinct computed field: the primary PF order parameter distinguishing solid (yellow) and liquid (cyan) regions, depicted in Fig. 9(b) (panels A1–A4). A representation of Iron (Fe) as a balancing element during segregation of alloying elements is illustrated in Fig. 9(b) (panels B1–B4). Fig. 9(b) (panels C1–C4 and D1–D4) denote partitioning of critical alloying elements in austenitic stainless steel i.e., Chromium (Cr) and Nickel (Ni), highlighting strong solute segregation behavior, respectively. Clearly visible Carbon (C) in Fig. 9(b) (panels E1–E4) segregates primarily in the interdendritic liquid during the $\delta - Fe$ growth at the initial solidification stage, in accordance with dendritic growth theory and the phase diagram [16]. In similar fashion Ni starts to segregate in the interdendritic region at t = 0.25 ms and this segregation gets stronger (red colored) as the microstructure evolves until t = 2 ms. Conversely, Cr is commonly reported as a $\delta - Fe$ former and contributes in the growth of solid leaving the interdendritic region Cr deficient. The variable concentration conditions give rise to two scenarios. Firstly, the local concentration difference lowers the local solidification temperature of the interdendritic liquid leaving it vulnerable to mechanical dissociation. Secondly, the unfavorable growth conditions at the interdendritic region give rise to the probability of the SDAs which actualize if there is sufficient space

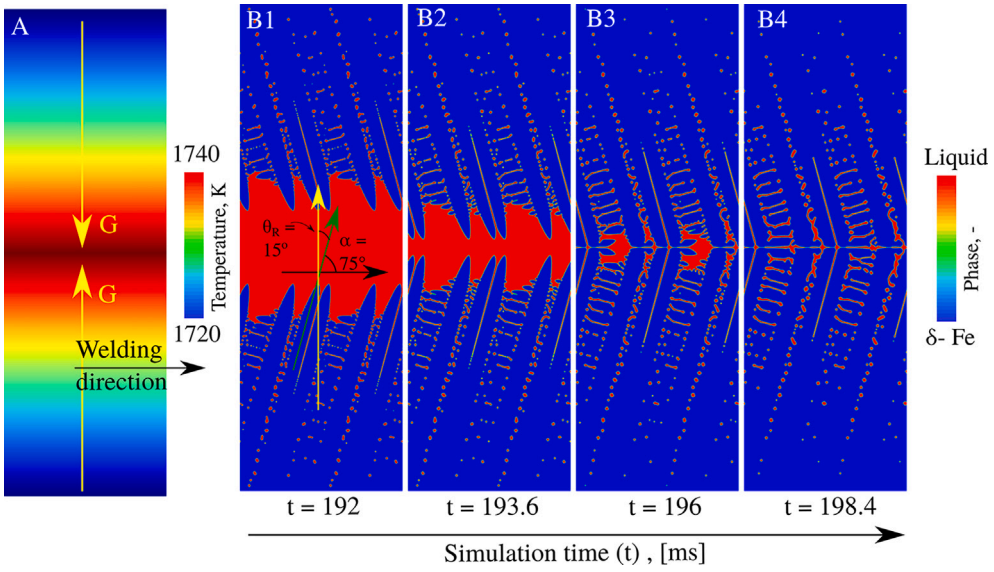

Fig. 10. Evolution of dendritic morphology along the centerline of weld seam during last stage of solidification under G = 50 K/mm (A) showing dendritic growth evolution at $\theta_R = 15°$ for t = 192 ms to t = 198.4 ms (B1–B4). Green, yellow and black arrows represent directions for dendrite growth along ⟨100⟩, G, and welding, respectively. (For interpretation of the references to color in this figure legend, the reader is referred to the web version of this article.)

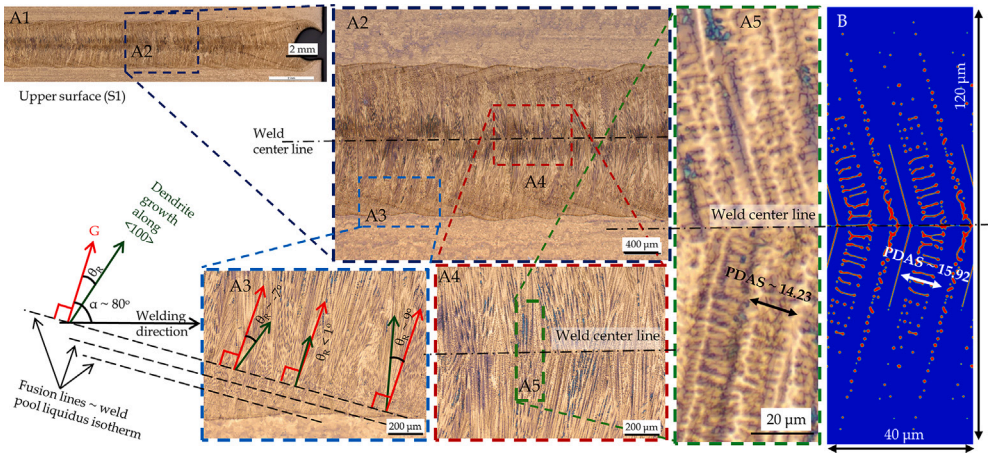

Fig. 11. Comparison of experimentally observed and PF simulated dendritic morphology in the upper surface (S1), refer to Fig. 2, showing (A1–A5) hierarchical optical micrographs revealing PDAS and (B) simulated dendritic morphology highlighting dendrite cores (blue) and interdendritic liquid (red), with quantitative agreement in PDAS. (For interpretation of the references to color in this figure legend, the reader is referred to the web version of this article.)

available as in case of high $\theta_R = 45°$ in the current case. Notably, the emergence of side-branching creates deep solute channels apparent in last stage of morphology evolution (B4–E4), signaling the morphological complexity.

3.1.4. Simulating the weld-center

Fig. 10 visualizes results from a 2D PF simulation of dendritic solidification at $\theta_R = 15°$, induced due to preferred crystal growth direction perpendicular to the macroscopic weld pool surface near the centerline of the weld. 2D dendrites are seen growing at $\alpha = 75°$, where α is an angle between dendrite's preferred growth direction i.e., ⟨100⟩ and the welding direction as highlighted in Fig. 10(B1). A linearly increasing G of 50 K/mm directed towards the center of the domain is applied in this simulation. A V_s of 10 mm/s is considered in this simulation. Fig. 10(B1–B4) depicts the temporal evolution of the PF order parameter (ϕ), where red denotes the liquid region and blue denotes solid $\delta - Fe$ dendrites.

At early stage Fig. 10(B1), a clearly visible columnar dendritic solid accompanied by the emergence of (SDAs) is observed growing towards the centerline. Progression from Fig. 10(B1 to B4) demonstrates classic morphological selection: PDAs progressing, new SDAs emerging and coarsening, and isolated solute-rich droplets entrapped in the interdendritic liquid as a consequence of interaction of the adjacent SDAs. PDAs and SDAs appearance and persistence along with the evolution of the solid–liquid interface, reflect the interplay between applied G, θ_R, local V_s, and interfacial energy anisotropy, consistent with established theories of dendritic growth [48].

3.1.5. Experimental validation at upper surface (S1)

Fig. 11 presents a multi-scale assessment of dendritic morphology, cross-validating experimental observations with multiphase-field simulation results to elucidate the representativeness of simulated microstructures under experimental local thermal conditions. Fig. 11(A1-A5) sequentially zooms from the full upper surface (S1) of the solidified

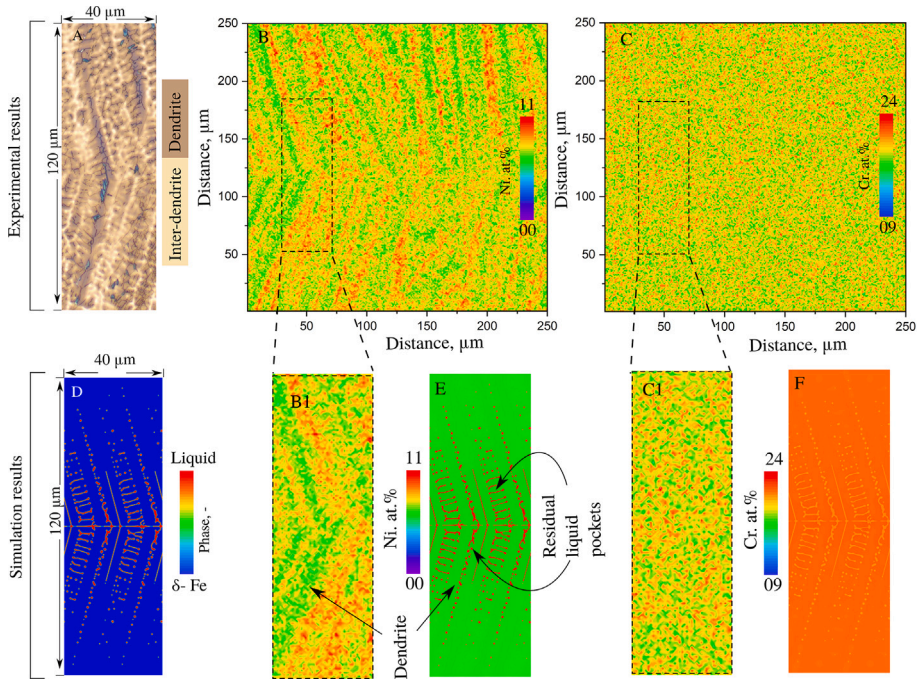

Fig. 12. Comparison of experimentally measured (A) and PF simulated (D) dendritic microstructures and solute segregation fields in a quaternary Fe–Cr–Ni–C alloy, highlighting spatial distributions of Ni (B and B1) and Cr (C and C1) concentrations across dendritic and interdendritic regions. Simulated solute segregation results for Ni (E) and Cr (F) are displayed for quantitative cross-comparison.

sample already depicted in Fig. 2 to finer spatial regimes for comparison purposes at micro-scale. Through multiple magnifications, various necessary observations are explained for clarity, indispensable for simulation studies to get comparable results. Intermediate-scale weld seam surface in Fig. 11(A2) displays multiple fusion lines along the boundary of the weld seam near fusion zone. This phenomenon is highlighted in Fig. 11(A3), where hardly visible fusion lines corresponding to weld pool liquidus isothermal surface are exaggerated to show the G direction during solidification. It is evident from various studies [10] that G—shown with red colored arrow—is always directed perpendicular to the fusion lines. The misorientation angle θ_R as a difference between the angle of G (red arrow) and the preferred crystal growth direction i.e., ⟨100⟩ (green arrow) is displayed for clarity. It is important to note that θ_R increases the probability of the SDAs in left and right most cases i.e., $-7°$ and 9° in Fig. 11(A3), respectively. Contrarily, the cellular dendrites grow without SDAs as shown in the middle case with $\theta_R < 1°$.

Fig. 11(A4) reveals the columnar array of PDAs solidified probably at θ_R of ± 15°, distinct SDAs, and highly anisotropic growth morphology with characteristic features of directional solidification in multi-component alloys under the influence of local G. Its magnified area in Fig. 11(A5) represents the columnar dendrites mostly with SDAs growing from the fusion lines and meeting at the weld centerline. An important measure for comparison of morphology with simulation results is PDAS, because the experimental observation of the R_{tip} and V_{tip} is technologically complicated especially for opaque alloys solidifying at very high temperatures, i.e., $T_0 > 1700$ K. Fig. 11(B) displays a phase map at last stage of solidification simulation from Fig. 10(B4), replicating the experimental, with solid dendrite cores rendered in blue and residual liquid outlined in red. The simulated microstructure reproduces not only the growth pattern and size of primary and secondary arms but also the PDAS, facilitating direct visual and quantitative comparison with the experimental micrographs. The PDAS value is a statistical average of the data points from both experimental observation (14.23 μm), shown in Fig. 11(A5) and simulation result (15.92 μm), displayed in Fig. 11(B), calculated using an image analysis software called ImageJ [54].

Fig. 12 displays experimental observations with 2D PF simulation results for dendritic solidification, elucidating both microstructural morphology and solute segregation patterns. Fig. 12(A) presents an optical micrograph of the solidified dendritic array with dendrite and interdendritic regions labeled with dark brown and light brown colors, respectively. Fig. 12(B and C) display spatially resolved experimental concentration maps of Ni (at.%) and Cr (at.%), respectively, acquired by high-resolution compositional analysis. Dashed rectangles demarcate regions subsequently shown at higher magnification in B1 (for Ni) and C1 (for Cr). Fig. 12(D–F) correspond to PF simulation outputs: D shows the phase map at later solidification stage, while E and F present simulated Ni and Cr concentration fields in at.% using identical color scales and concentration distribution ranges as in the experimental maps.

The experimental data reveal pronounced Ni enrichment in interdendritic channels relative to dendrite cores, while Cr appears more uniformly distributed, consistent with differences in partition coefficients of the respective solutes. The PF model quantitatively reproduces these solute segregation trends, capturing the PDAS and the alternating Ni-rich inter-dendrite and Ni-deficient dendrite contrast. The close agreement between simulated (E, F) and experimental (B1, C1) concentration fields for Ni and Cr respectively, particularly in the location and magnitude of the Ni enrichment, demonstrates the model's capacity to resolve solute transport and partitioning under the applied thermal gradients. Microstructure evolution under low thermal gradients is normally associated with central and vertically middle region of the weld seam [55]. Therefore, a simulation is designed with G = 0 K/mm and with no external pulling velocity applied to the growing dendrites. This means that whole domain has the same temperature of 1738 K and the driving force for dendritic solidification is provided by the solutal undercooling. The uni-directional growth of the dendrites is only because of the cubic anisotropy at the solid-liquid interface. The evolution of the dendritic microstructure at various times is observed in Fig. 13 at t = 0.6 ms to t = 16.6 ms from A1 to A5 while experimental observation of microstructure is shown for morphological comparison in Fig. 13(B). At initial stage of solidification (t = 0.6 ms) three seeds are observes on

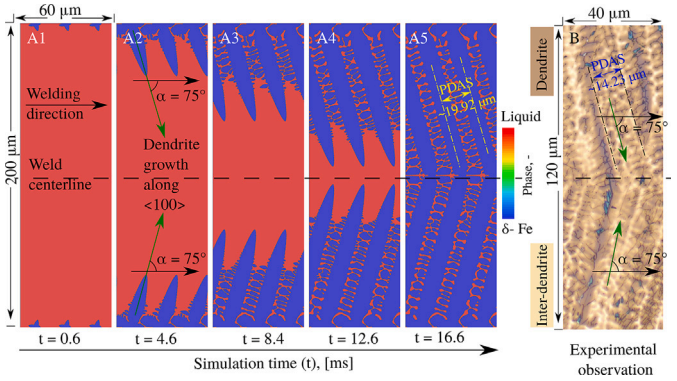

Fig. 13. Evolution of dendritic morphology along the centerline of weld during solidification under G = 0 K/mm, corresponding to t = 0.6 ms to t = 16.6 ms (A1–A5). Experimental observation of the dendritic structure at upper surface (S1) for morphological comparison (B).

top and bottom edges in the 2D domain growing at $\alpha = 75°$, while α is an angle between dendrite preferred growth direction i.e., ⟨ 100 ⟩ and the welding direction. SDAs arms are observed growing from the initial stage till t = 16.6 ms when the PDAs coincide and mutually merge at the weld centerline. A common phenomena of liquid entrapment between the PDAs is observed uniformly within the interdendritic region in the simulation results. PDAS in the simulation results recorded at the last stage is 19.92 µm while the same in experimental observation at S1 is recorded 14.23 µm. Although the appearance of the SDAs is comparable with the experimental observation in Fig. 13(B) due to growth at same angle, still there exists a difference in PDAS.

3.1.6. Experimental validation at middle surface S2

Fig. 14 presents a comprehensive multi-scale optical microscopy analysis of the lower cross-section from a directionally solidified steel sample processed with LBW, providing insight into the evolution and spatial arrangement of dendritic microstructures under experimentally relevant thermal gradients. Fig. 14(A) displays a low-magnification view capturing the overall weld pool geometry and highlighting the macroscopic boundary region where columnar dendritic growth is observed. Fig. 14(A1–A2) zooms into the solidification front, clearly detailing the dense network of aligned PDAs characteristic of high G and R conditions typical near the fusion boundary. Fig. 14(A3) further resolves the microstructure, illustrating the fine-scale spatial arrangement and confinement of truncated PDAs, cross-sectioned during micrography. The pronounced parallel alignment of PDAs with the imposed G near the centerline of the weld seam, is in line with established PF predictions for strong G–R regimes during directional solidification [56]. Fig. 14(A4) highlights the sub-micron interdendritic regions showcasing the fully solidified arrangement of dendrites in dark color and interdendritic region in light colors. The truncated PDAs indicate that the growth direction must have been almost perpendicular to the cross-sectional place. This observation demands that a 3D PF simulation result is necessary to study the morphological parameters of the dendrites and the liquid in the inter-dendritic region. To summarize, the 2D phase-field simulations, enabled by the automated Kadi4Mat workflow and PACE3D solver, effectively capture weld pool microstructure evolution by segmenting the 3D domain into feasible sub-domains with periodic boundaries. Key findings reveal a G threshold below ≈700 K/mm for stable solidification, monotonic decreases in (R_{tip}) with rising G and R, peaking dendrite density under high G–R, and finer PDAS. These features are validated by experimental PDAS (14–20 µm agreement) and solute segregation of Ni and Cr on surfaces S1 and S2. Misorientation θ_R critically drives growth competition, SDA formation, and morphological instability, with favorably aligned ⟨ 100 ⟩ grains dominating near the centerline, bridging local thermal conditions in LBW to realistic microstructure patterns.

3.2. Phase-field simulation results in 3D

To study the morphology of liquid, entrapped within the grown dendrites at various θ_R, a set of simulations is designed with $\theta_R = 0°$ to 45° with an increment of $\theta_R = 15°$ as shown in Fig. 15. Fig. 15(A and B) presents the $\theta_R = 45°$ where grown dendrites with entrapped liquid are shown with blue and red colors displaying side view and isometric view for better visualization, respectively. Fig. 15(C) shows the morphology of the liquid entrapped during the growth process of solid dendrites into bulk liquid. Similarly all the other cases of θ_R i.e., 30°, 15° and 0° are displayed in Fig. 15(D–F), (G–I) and (J–L) respectively. The local thermal condition i.e., G = 50 K/mm is imposed in such a way that the temperature in the domain increases linearly in an upward direction (positive x-direction/welding direction). As the periodic boundary conditions are used on y and z boundaries, the domain is appended in y direction. For 45°, there exists an equal driving force to choose rightward or leftward growth of dendrites. As a result, both directions are observed with secondary dendrites being more prominent as this case in shown in Fig. 15(A). The liquid in Fig. 15(C) shows both continuous liquid films and entrapped liquid pockets corresponding to the mix of columnar and cellular dendrites in the structure. For $\theta_R = 30°$ and 15° the dendrite tips are seen as non-spherical and grow more in the lateral direction due to significant G values. In all the lower three θ_R values

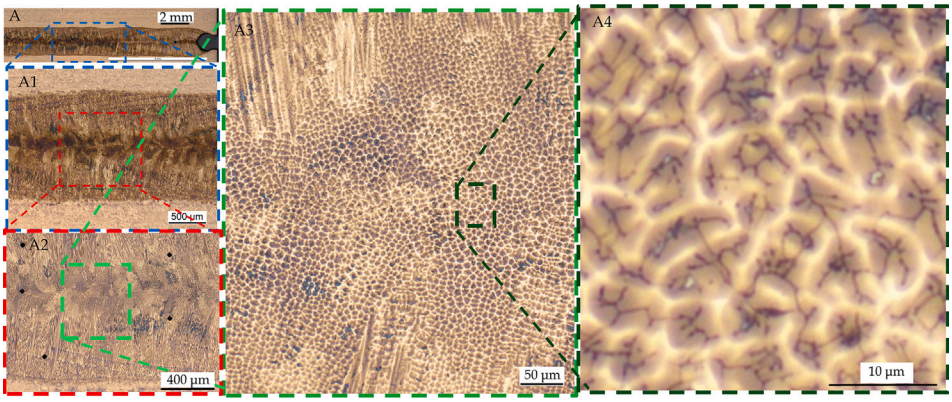

Fig. 14. Hierarchical optical micrographs of the middle surface (S2) (refer Fig. 2) in a solidified sample presenting multi-length-scale dendritic morphology, from the macroscopic weld seam (A), through branching and dense arrays of truncated PDAs along the centerline of the weld seam at different magnifications (A1–A3), down to sub-micron interdendritic features (A4).

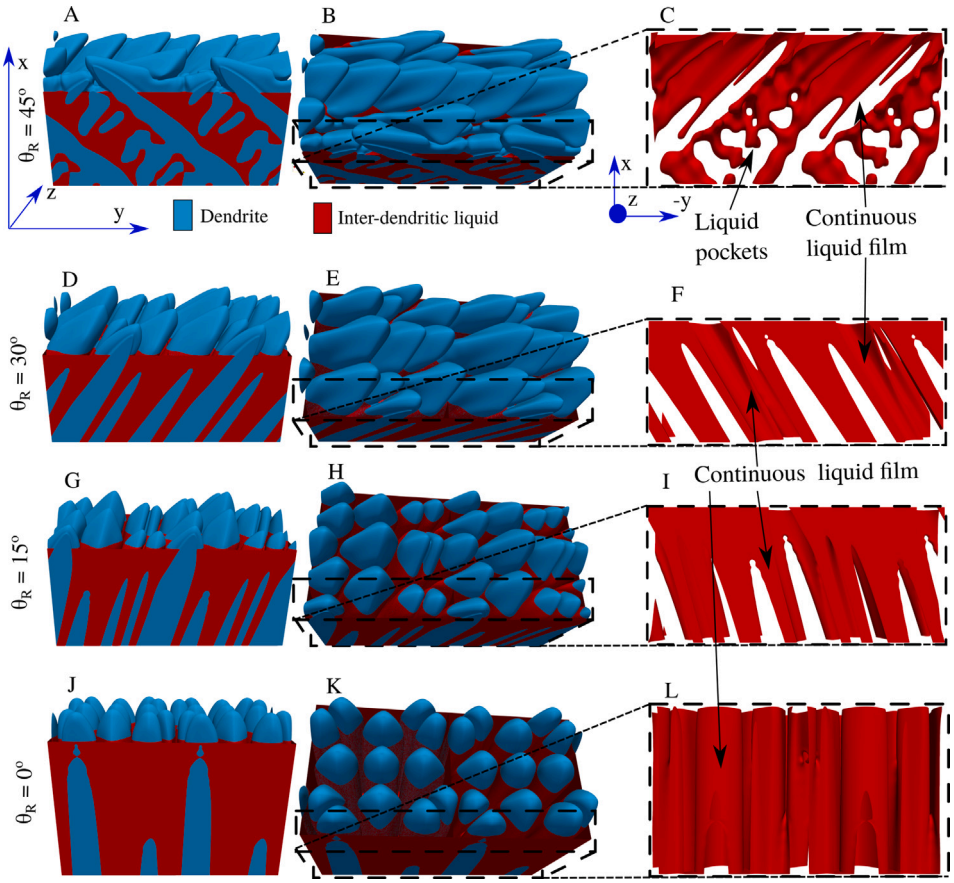

Fig. 15. 3D PF simulation results illustrating the dendritic and liquid morphologies swept during growth at θ_R = 45° (A–C), 30° (D–F), 15° (G–I), and 0° (J–L), respectively.

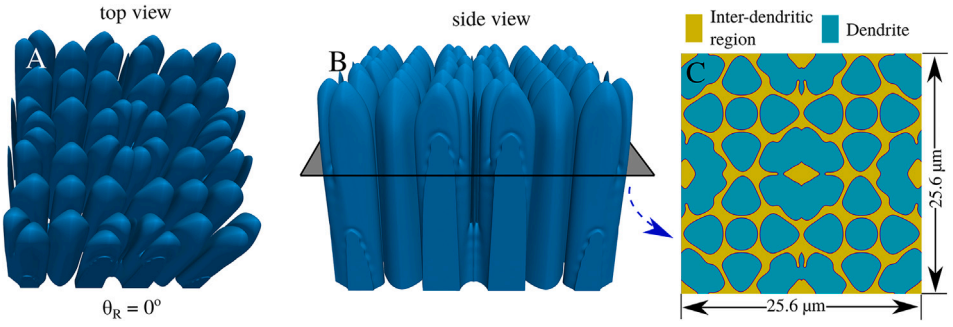

Fig. 16. 3D PF simulation of alloy solidification showing an isometric view of the dendrite array (A), a side view with an indicated cross-sectional plane (B), and the corresponding 2D cross-section distinguishing solid (cyan) and liquid (yellow) (C), revealing columnar PDAs and corresponding PDAS. (For interpretation of the references to color in this figure legend, the reader is referred to the web version of this article.).

the cellular dendrites without any SDAs are observed as in case of 2D simulation results shown in Fig. 9(a). The liquid entrapped in these dendrites is always in the form of thin films which run from bottom to the dendrite tip.

As evident from Fig. 14(A3), most of the dendrite trunks are seen to grow perpendicular to the surface, an interesting case for further study is with θ_R = 0°, which is considered in Fig. 16. The progressive morphological evolution—from early compact dendrites with multiple primary seeds, to the later-stage with grown PDAs refer to Fig. 16(A)—demonstrates the competition between tip advancement, PDA coarsening, and disappearance of side-branching instabilities. The simulations resolve the 3D interfacial topology without explicit surface tracking, capturing both tip advancement and PDA thickening phenomena characteristic of alloy dendritic solidification. In Fig. 16(A), the rendered 3D perspective captures the columnar dendrite trunks as they evolve from the solidification front, highlighting competitive growth and alignment along the gradient direction. Fig. 16(B) provides a side view of the same structure, explicitly indicating the location of a slice used to obtain the cross-sectional visualization. Fig. 16(C) displays the simulated cross-section on the highlighted cross-sectional plane, where the spatial partitioning between solid (cyan) and liquid (yellow) regions delineates the primary dendrite array and inter-dendritic liquid channels, respectively. Quantitatively, the observed evolution reflects the system's sensitivity to imposed G and R. Morphological attributes such as the

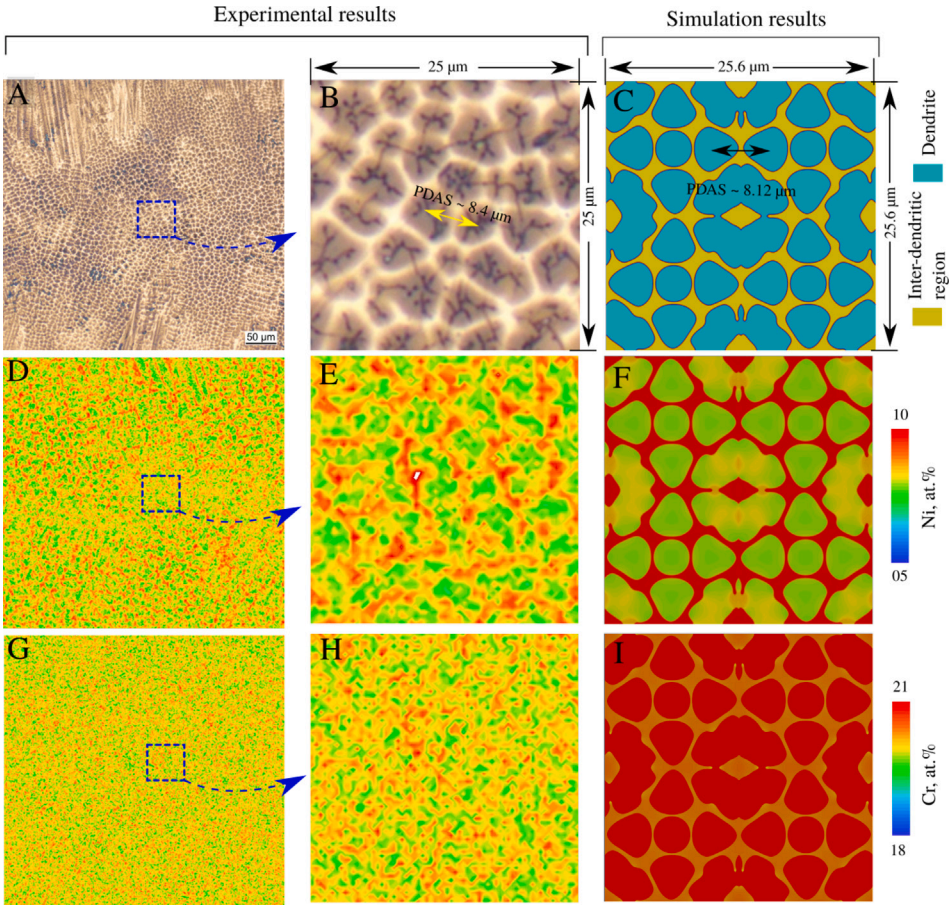

Fig. 17. Direct comparison of experimentally measured and PF simulated dendritic microstructure illustrating PDAS (A-C) and solute segregation in a representative transverse cross-section for critical alloying elements i.e., Ni (D-F) and Cr (G-I) in both experimental and simulated results.

PDAS and R_{tip}, extracted from such slices, serve as direct metrics for comparison to experimental microstructures produced under analogous thermal regimes. The strong alignment and regularity of dendrite trunks reflect the directional thermal gradient, but local variations in dendrite width and side-branching suggest subtle influences of solutal effects, which are further discussed in Fig. 17.

3.2.1. Experimental comparison at S2

Fig. 17 compares the dendritic microstructure and solute segregation patterns obtained experimentally and by PF simulations for a quaternary Fe–Cr–Ni–C alloy. Fig. 17(A–C) shows the morphological agreement between experiment (A: EPMA; B: region magnified from A) and simulation (C: phase-field; cyan: dendrite, yellow: inter-dendritic liquid). When the PDAS from the experimentally observed S2 (i.e., 8.4 µm) is compared with the statistically analyzed PDAS from the simulation results (i.e., 8.12 µm), a quantitative validation is obtained. The dendritic network and characteristic cellular arrangements observed experimentally are quantitatively reproduced, indicating the ability of the PF approach to capture microstructural length scales driven by imposed solidification conditions.

Fig. 17(D–F) and (G–I) quantitatively compare the spatial distribution of Ni and Cr with emphasis on solute-rich channels and microsegregation features that arise from solutal partitioning of Ni and Cr during late-stage solidification, respectively. Experimental EPMA maps (D, E, G, H) are shown alongside PF results (F, I), both using same scale color bars to show relative concentration fields. Insets highlight local segregation features and demonstrate the agreement in both amplitude and spatial distribution of solute partitioning across dendrite and inter-dendrite regions. Simulations largely align with experimentally measured segregation patterns, lending support to the thermodynamic and kinetic model assumptions in this multi-component system. These quantitative features are critical in determining local compositional inhomogeneity and potential sites of defect nucleation or phase transformation.

To summarize, 3D phase-field simulations reveal that increasing θ_R from 0° to 45° promotes rapid dendrite tip advancement at low θ_R, transitioning to enhanced lateral growth, SDA development, and complex liquid entrapment at higher θ_R. At $\theta_R = 0°$, columnar PDAs form with thin interdendritic liquid films, aligning perpendicular to the solidification front under G = 50 K/mm. Quantitative validation against experiments at surface S2 shows excellent agreement in PDAS (8.12 µm simulated against 8.4 µm experimental) and solute segregation patterns for Ni, confirming the model's accuracy in capturing 3D morphological and microsegregation effects.

4. Discussion

In order to analyze the mechanical performance i.e., resistance to solidification cracking of the weld seam during early stage of solidification, the focus must be kept on the growth of dendritic structures i.e., preferred growth direction, PDAS, and appearance of the SDAs resulting in the entrapped liquid. An important factor in determining these structural parameters is the weld pool shape [5,57], corresponding V_s and local G experienced by the growing dendrites. Very high G values associated with the LBW ranging upto 5000 K/mm are commonly reported in the literature for various alloys [58], which are true when whole weld pool at macroscopic level is considered. It is also reported

that larger G values appear along the fusion line due to a large amount of heat transferred to adjacent low temperature unmelted solid grains, resulting in rapid solidification conditions unlike the lower G values near centerline further away from the fusion line resulting in steady state quasi-equilibrium solidification conditions [49]. The actual G values relevant for the solidification cracking defect based on microstructure developed along the centerline of the weld-seam are indeed at least 2 orders of magnitude smaller i.e., 75 K/mm [59]. This is presented with the PDAS comparison from experimental observation and simulation results in Fig. 11 showing a difference of only 1.69 μm with G = 50 K/mm. On the other hand a comparatively large PDAS difference i.e., ≈6 μm is observed when simulations are carried out with G = 0 K/mm, illustrated in Fig. 13, supporting the argument that completely ignoring the local G produces physically incomparable results.

The hypothesis for G = 0 K/mm originated from the observation of the microstructural features near the centerline of the weld seam resembling the equiaxed dendrites from the cross-section shown in Fig. 14(A3 and A4). There could be only two reasons for this observation. Firstly, the cross-section shows the truncated columnar dendrites which must have grown under $G \neq 0$ or directional solidification conditions from the bottom of the weld towards the top surface. Secondly, according to the weld pool surface shown in Fig. 3(B and C), the solidifying liquid near the centerline at the middle surface S2 (refer to Fig. 2) should have experienced $G \approx 0$, avoiding directional solidification, giving rise to equiaxed dendrite morphology displayed in the cross-section in Fig. 14(A3 and A4). The latter does not seem to be the case, firstly because of the comparatively large difference in PDAS between experimental observation and simulation results at $G \approx 0$. Secondly the vertically growing columnar grains have been observed with Electron Back-scatter Diffraction (EBSD) images during LBW by Ushmaev et al. [60]. Staying with the former assumption the 3D simulation results produce well-comparable results with the experimental observations both for morphology and the microsegregation.

Appearance of the solidification cracks is associated not only with the rupture of continuous liquid film between the dendrites during solidification shrinkage but also with the entrapped liquid pockets responsible for structural inhomogeneity due to mechanically unfeasible microsegregation resulting in delayed solidification [11]. The former case is more dominantly associated with the cellular-dendrites growing parallel to the laser beam velocity lacking SDAs as shown by 2D and 3D simulation results in Fig. 9(a) up to $\theta_R = 30°$ and Fig. 15, respectively. The latter case is accompanied by the dendrite colonies developing towards the weld centerline during early stage of solidification with a combination of PDAs and SDAs giving rise to the entrapment of discontinuous liquid pockets. This phenomenon is observed at higher θ_R in 2D and 3D simulations as in Figs. 9(b), 10, 13 and 15. Therefore, for SDAs' appearance, the effects of V_s and G are not sufficient to characterize the parameter space; rather θ_R must also be considered for better microstructure prediction.

The competitive grain growth behavior shown in Fig. 8 is a canonical phenomenon in directional solidification metallurgy, first systematically described by Walton & Chalmers [52] and subsequently formalised within the probabilistic microstructure selection framework of Rappaz & Gandin [50,51]. The Walton–Chalmers selection criterion states that, during competitive columnar growth, grains whose ⟨100⟩ preferred growth direction is most closely aligned with the local thermal gradient will progressively overgrow grains with larger misorientation, because favourably oriented grains sustain a lower kinetic undercooling at the solidification front. Fig. 8 precisely illustrates this selection: grains with $\theta_R = 45°$ are progressively eliminated, while those with $\theta_R = 0°$ dominate the later-stage microstructure. This behavior emerges naturally from the orientation-dependent anisotropy function $a_c(\boldsymbol{q}^{roi}_{\alpha\beta}(\theta_{\alpha\beta}))$ (Eq. (13)) in the PF model, which penalises growth in non-⟨100⟩ directions through the rotation matrix $\boldsymbol{R}_{\alpha\beta}(\theta_{\alpha\beta})$—a direct mathematical encoding of the Walton–Chalmers physics.

The probabilistic cellular automaton (CA) model of Rappaz and Gandin [50,51] predicts that the final texture at the weld centerline is determined by successive competitive elimination of unfavourably oriented grains. Current simulations confirm this prediction within the PF framework. While both Walton–Chalmers and Rappaz–Gandin frameworks address grain-level orientation selection, they do not resolve SDA morphology or inter-dendritic liquid topology during competition. Current PF simulations demonstrate that θ_R not only governs competitive grain elimination but also fundamentally alters SDA formation (Figs. 9(a) and 15) and the 3D topology of entrapped liquid. This information has direct relevance to solidification cracking susceptibility that is inaccessible to CA-based models.

The 2D parametric study (Sections 3.1.2 and 3.1.3) serves a well-defined purpose to systematically map the microstructural response surfaces: (PDAS, R_{tip}, dendrite number density, morphological transitions) across the full (G, V_s, θ_R) parameter space. This task would be computationally prohibitive in full 3D. However, 2D simulations carry three important limitations: Firstly, the 3D results (Fig. 15) reveal a rich topology of inter-dendritic liquid—ranging from continuous thin films at low θ_R to isolated pockets at high θ_R, which is not fully reproducible in 2D. 2D simulations represent liquid films as continuous channels irrespective of crystallographic orientation, potentially underestimating isolated pocket formation, which has a direct bearing on solidification cracking susceptibility. Secondly, Gibbs–Thomson undercooling and capillary-driven morphological selection depend on the full mean curvature in 3D. Thirdly, 2D simulations neglect out-of-plane curvature contributions, introducing quantitative errors in the predicted R_{tip} and PDAS even when qualitative morphological trends are faithfully captured. The 3D simulations in this study are therefore used to validate and extend the 2D parametric trends for selected conditions most relevant to the experimental observations (Section 3.2.1). This complementary 2D–3D strategy is consistent with established practice in the computational materials modeling community for various applications [61].

The misorientation angle θ_R cannot be directly controlled as a process input, but emerges from the interaction between base-material grain texture and the local heat-flow direction at the fusion boundary. Practical controllable factors on the effective θ_R distribution include beam oscillation, which randomizes the heat-flow direction and prevents dominant low-θ_R columnar textures. Moreover, thermomechanical pretreatment can orient ⟨100⟩ grains preferentially along the heat-flow direction. Alternatively, EBSD-guided welding, where pre-weld texture characterization allows prediction and control of the θ_R distribution via welding direction or beam angle adjustment or grain refinement by inoculation, which disrupts persistent columnar growth. A comprehensive validation against experimentally measured EBSD maps of the solidified weld cross-sections (S1 and S2) is planned as the direct next step, targeting quantitative comparison of grain orientation distributions and competitive grain elimination patterns beyond the PDAS-level validation presented here.

Microsegregation of alloying elements i.e., Ni and Cr predicted by the PF model is validated quantitatively with the experimental observations. For Ni, the comparison in both 2D and 3D results presents a well comparable quantitative and visual data. Ni being an Austenite former segregates to the interdendritic region [62]. This microsegregation is well captured by the 2D and 3D PF model. Conversely, the Cr being $\delta - Fe$ former is distributed within the dendrites without a significant quantitative difference between liquid and solid due to very close equilibrium compositions therein. This effect is observed in the magnified experimental image in Fig. 17(H). However, for better comparison a highly resolved experimental observation would serve the purpose in a better way. Similarly, consideration of unmodeled kinetic effects e.g., back-diffusion would help the model to calculate the microsegregation in an even more realistic way. The obtained insights gained from dendritic growth analysis in this study will serve as input

to a chemo-thermo-mechanically coupled PF model, supporting more accurate prediction of solidification cracking and facilitating optimized alloy design.

5. Conclusions

By integrating thermocouple-validated CFD modelling, CALPHAD-based phase-field simulations, and a Kadi4Mat-automated parametric workflow, this study establishes a quantitative, FAIR-compliant framework for predicting solidification microstructure in LBW of EN 1.4301 stainless steel. The four specific contributions of this work are:

1. A Kadi4Mat-integrated automated workflow for systematic, large-scale PF simulation studies of dendritic solidification in LBW is presented and validated, managing > 160 simulations while ensuring FAIR-compliant data management and substantially reducing manual pre-processing effort.
2. Systematic 2D PF simulations across the (G, V_s, θ_R) parameter space yield quantitative response surfaces for PDAS, R_{tip}, and morphological selection, providing a comprehensive microstructural map applicable to the full range of thermal conditions present along the weld-pool boundary.
3. The misorientation angle θ_R is identified as a fundamental parameter—alongside G and V_s—governing the transition between cellular and dendritic morphologies, the development of secondary dendrite arms, and the topology of inter-dendritic liquid (continuous films versus isolated pockets), with direct implications for solidification cracking susceptibility. Specifically, both extremes of θ_R carry distinct SC risk pathways: continuous thin films at low $\theta_R \leq 15°$, and isolated liquid pockets at high $\theta_R \geq 30°$.
4. Quantitative agreement between simulated and experimentally measured PDAS (< 12% deviation at S1; < 4% at S2) and spatially resolved solute segregation patterns (Ni and Cr) validates the phase-field model and CALPHAD-based thermodynamic description for the quaternary EN 1.4301 alloy under LBW conditions.

The present results provide a vivid picture of how local thermal conditions and grain orientation jointly govern the cellular–dendritic morphology selection in LBW. They identify two concrete process levers for microstructural defect control in industrial practice: *beam oscillation* to randomise the local heat-flow direction at the fusion boundary; *heat-input selection* guided by the (G, V_s) response maps (Fig. 7). It would nevertheless be premature to formulate concrete process instructions at this stage, because the quantitative link between the simulated solidification microstructure and solidification-cracking initiation requires a coupled chemo-thermo-mechanical analysis of the simulation domains, validated against experimental crack observations.

CRediT authorship contribution statement

Muhammad Umar: Writing – review & editing, Writing – original draft, Visualization, Validation, Software, Methodology, Investigation, Formal analysis, Data curation, Conceptualization. **Ahmed Elmoghazy:** Validation, Software, Methodology. **Andrey Gumenyuk:** Writing – review & editing, Writing – original draft, Software, Investigation, Data curation, Conceptualization. **Nasim Bakir:** Formal analysis, Data curation, Conceptualization. **Daniel Schneider:** Writing – review & editing, Validation, Supervision, Resources, Project administration, Methodology, Funding acquisition, Conceptualization. **Britta Nestler:** Writing – review & editing, Validation, Supervision, Software, Resources, Methodology, Funding acquisition, Conceptualization. **Michael Rethmeier:** Writing – review & editing, Supervision, Resources, Project administration, Funding acquisition, Conceptualization. **Michael Schmidt:** Writing – review & editing, Validation, Supervision, Resources, Project administration, Methodology, Funding acquisition, Conceptualization.

Declaration of competing interest

The authors declare that they have no known competing financial interests or personal relationships that could have appeared to influence the work reported in this paper.

Acknowledgements

The authors gratefully acknowledge the main financial support of the German Research Foundation (DFG) in the framework of project no. 434946896 within the research unit FOR5134, (TP-1 and TP-6) “Erstarrungsrisse beim Laserstrahlschweißen: Hochleistungsrechnen für Hochleistungsprozesse - Mikrostruktursimulation der Erstarrung in der Schweißnaht”. The authors acknowledge support by the state of Baden-Württemberg through bwHPC. Provision of carefully calculated CALPHAD database for the quaternary alloy (Fe-Cr-C-Ni) by research group of Prof. Chong Chen from Henan University of Science and Technology, Luoyang, China is thankfully acknowledged. The authors are grateful for providing the EPMA measurements, which were conducted by Ms. Gabriele Oder from Dept. 5.1 Bundesanstalt für Materialforschung und -prüfung. Furthermore, funding by the Helmholtz Association through the programme “MSE”, no. 43.31.01 was provided.

Data availability

Data will be made available on request.

References

[1] A. Otto, H. Koch, K.-H. Leitz, M. Schmidt, Numerical simulations - a versatile approach for better understanding dynamics in laser material processing, Phys. Procedia 12, Part A (2011) 11–20, lasers in Manufacturing 2011 - Proceedings of the Sixth International WLT Conference on Lasers in Manufacturing.
[2] S. Katayama, Handbook of Laser Welding Technologies, Elsevier, 2013.
[3] F. Qayyum, M. Umar, V. Elagin, M. Kirschner, F. Hoffmann, S. Guk, U. Prahl, Influence of non-metallic inclusions on local deformation and damage behavior of modified 16mncrs5 steel, Crystals 12 (2) (2022) 281.
[4] M. Umar, F. Qayyum, M.U. Farooq, S. Guk, U. Prahl, Qualitative investigation of damage initiation at meso-scale in spheroidized c45ec steels by using crystal plasticity-based numerical simulations, J. Compos. Sci. 5 (8) (2021) 222.
[5] C. Li, X. Li, Y. Zhang, K. Wen, L. Yan, Y. Li, Y. Li, M. Yu, G. Gao, H. Yan, Z. Li, B. Xiong, Achieving high strength and good laser welding performance by adding SC to t8-aged al-cu-li alloys with different cu/li ratios, Mater. Des. 256 (2025) 114285, https://doi.org/10.1016/j.matdes.2025.114285, https://www.sciencedirect.com/science/article/pii/S0264127525007051.
[6] M. Umar, F. Qayyum, M.U. Farooq, L.A. Khan, S. Guk, U. Prahl, Investigating the effect of cementite particle size and distribution on local stress and strain evolution in spheroidized medium carbon steels using crystal plasticity-based numerical simulations, Steel Res. Int. 92 (3) (2021) 2000407.
[7] T. Takaki, Phase-field modeling and simulations of dendrite growth, ISIJ Int. 54 (2) (2014) 437–444, https://doi.org/10.2355/isijinternational.54.437
[8] W.L. George, J.A. Warren, A parallel 3D dendritic growth simulator using the phase-field method, J. Comput. Phys. 177 (2) (2002) 264–283.
[9] G. Agarwal, A. Kumar, I. Richardson, M. Hermans, Evaluation of solidification cracking susceptibility during laser welding in advanced high strength automotive steels, Mater. Des. 183 (2019) 108104, https://doi.org/10.1016/j.matdes.2019.108104, https://www.sciencedirect.com/science/article/pii/S0264127519305428.
[10] S. Tiwari, S. Ghosh, Orientation selection in alloy dendritic evolution during melt-pool solidification, Comput. Mater. Sci. 249 (2025) 113664.
[11] G.-W. Park, S. Shin, J.-Y. Kim, Y.-M. Koo, W. Lee, K.-A. Lee, S.S. Park, J.B. Jeon, Analysis of solidification microstructure and cracking mechanism of a matrix high-speed steel deposited using directed-energy deposition, J. Alloys Compd. 907 (2022) 164523.
[12] C. Yang, F. Yang, X. Meng, S.N. Putra, M. Bachmann, M. Rethmeier, Phase-field simulation of the dendrite growth in aluminum alloy aa5754 during alternating current electromagnetic stirring laser beam welding, Int. J. Heat Mass Transf. 218 (2024) 124754.
[13] J. Warren, W. Boettinger, Prediction of dendritic growth and microsegregation patterns in a binary alloy using the phase-field method, Acta Metall. Mater. 43 (2) (1995) 689–703, https://doi.org/10.1016/0956-7151(94)00285-P, http://www.sciencedirect.com/science/article/pii/095671519400285P.
[14] K. IAM-MMS, Phase-field algorithms for computational engineering (Pace3D), 2025. https://www.iam.kit.edu/mms/english/5317.php (Accessed 11 February 2026).
[15] J. Hötzer, A. Reiter, H. Hierl, P. Steinmetz, M. Selzer, B. Nestler, The parallel multi-physics phase-field framework PACE3D, J. Comput. Sci. 26 (2018) 1–12.

[16] M. Umar, M. Seiz, M. Kellner, B. Nestler, D. Schneider, Solidification of a quaternary x5crni18-10 alloy during laser beam welding using calphad data in a phase-field approach, Comput. Mater. Sci. 249 (2025) 113627.
[17] K.D. Noubary, M. Kellner, J. Hötzer, M. Seiz, H.J. Seifert, B. Nestler, Data workflow to incorporate thermodynamic energies from calphad databases into grand-potential-based phase-field models, J. Mater. Sci. 56 (20) (2021) 11932–11952, https://doi.org/10.1007/s10853-021-06033-7
[18] A. Choudhury, B. Nestler, Grand-potential formulation for multicomponent phase transformations combined with thin-interface asymptotics of the double-obstacle potential, Phys. Rev. E 85 (2) (2012) 021602.
[19] J.P. Oliveira, A. Shamsolhodaei, J. Shen, J. Lopes, R. Gonçalves, M. de Brito Ferraz, L. Piçarra, Z. Zeng, N. Schell, N. Zhou, et al., Improving the ductility in laser welded joints of cocrfemnni high entropy alloy to 316 stainless steel, Mater. Des. 219 (2022) 110717.
[20] T. DebRoy, H.L. Wei, J.S. Zuback, T. Mukherjee, J.W. Elmer, J.O. Milewski, A.M. Beese, A.D. Wilson-Heid, A. De, W. Zhang, Additive manufacturing of metallic components–process, structure and properties, Prog. Mater. Sci. 92 (2018) 112–224.
[21] P. Collins, D. Brice, P. Samimi, I. Ghamarian, H. Fraser, Microstructural control of additively manufactured metallic materials, Annu. Rev. Mater. Res. 46 (1) (2016) 63–91.
[22] S. Akamatsu, G. Faivre, Anisotropy-driven dynamics of cellular fronts in directional solidification in thin samples, Phys. Rev. E 58 (3) (1998) 3302.
[23] S. Li, H. Xiao, K. Liu, W. Xiao, Y. Li, X. Han, J. Mazumder, L. Song, Melt-pool motion, temperature variation and dendritic morphology of inconel 718 during pulsed-and continuous-wave laser additive manufacturing: a comparative study, Mater. Des. 119 (2017) 351–360.
[24] E. Saccenti, M.E. Timmerman, J. Camacho, A simulation study of the effects of additive, multiplicative, correlated, and uncorrelated errors on principal component analysis, J. Chemom. 38 (12) (2024) e3595.
[25] B. Flemisch, S. Hermann, M. Herschel, D. Pflüger, J. Pleiss, J. Range, S. Roy, M. Takamoto, B. Uekermann, Research data management in simulation science: infrastructure, tools, and applications, Datenbank-Spektrum (2024) 1–9.
[26] S. Musslick, L.K. Bartlett, S.H. Chandramouli, M. Dubova, F. Gobet, T.L. Griffiths, J. Hullman, R.D. King, J.N. Kutz, C.G. Lucas, et al., Automating the practice of science: opportunities, challenges, and implications, Proc. Natl. Acad. Sci. 122 (5) (2025) e2401238121.
[27] S. Mahapatra, D.S. Ivanov, S.R. Hallett, J.P.-H. Belnoue, Numerical simulation of process-induced defects in thermosetting automated fibre placement (AFP): a review, composites Part A, Appl. Sci. Manuf. (2025) 109265.
[28] C. Draxl, M. Scheffler, Big Data-Driven Materials Science and Its FAIR Data Infrastructure, Springer International Publishing, Cham, 2020.
[29] N. Brandt, L. Griem, C. Herrmann, E. Schoof, G. Tosato, Y. Zhao, P. Zschumme, M. Selzer, Kadi4mat: a research data infrastructure for materials science, Data Sci. J. 20 (2021) 8.
[30] L. Griem, P. Zschumme, M. Laqua, N. Brandt, E. Schoof, P. Altschuh, M. Selzer, Kadistudio: fair modelling of scientific research processes, Data Sci. J. 21 (2022) 16.
[31] G. Pizzi, A. Cepellotti, R. Sabatini, N. Marzari, B. Kozinsky, AiiDA: automated interactive infrastructure and database for computational science, Comput. Mater. Sci. 111 (2016) 218–230, https://doi.org/10.1016/j.commatsci.2015.09.013, https://www.sciencedirect.com/science/article/pii/S0927025615005820.
[32] R.M. Gorman, H.J. Oliver, Automated model optimisation using the cylc workflow engine (cyclops v1. 0), Geosci. Model Dev. 11 (6) (2018) 2153–2173.
[33] S. Bhatnagar, An agentic AI workflow to simplify parameter estimation of complex differential equation systems, arXiv preprint arXiv:2509.07283, 2025.
[34] P. Hartwig, N. Bakir, L. Scheunemann, A. Gumenyuk, J. Schröder, M. Rethmeier, A physically motivated heat source model for laser beam welding, Metals 14 (2024) 430.
[35] M. Umar, V. Pavan Laxmipathy, D. Schneider, M. Selzer, B. Nestler, Role of interfacial surface anisotropy on liquid grooving at grain boundaries: a phase-field study, J. Appl. Phys. 137 (11) (2025).
[36] W. Liu, C. Chen, Y. Tang, Q. Long, S. Wei, G. Zhang, F. Mao, Q. Jiang, T. Zhang, M. Liu, Thermodynamic evaluation and investigation of solidification microstructure in the Fe–Cr–Ni–C system, CALPHAD 69 (2020) 101763.
[37] M. Segawa, A. Yamanaka, Multi-phase-field simulation of non-equilibrium solidification in 316 l stainless steel under rapid cooling condition, Mater. Trans. 64 (6) (2023) 1160–1168.
[38] M.J. Aziz, W. Boettinger, On the transition from short-range diffusion-limited to collision-limited growth in alloy solidification, Acta Metall. Mater. 42 (2) (1994) 527–537.
[39] D. Danilov, B. Nestler, Phase-field modelling of solute trapping during rapid solidification of a Si–as alloy, Acta Mater. 54 (18) (2006) 4659–4664.
[40] S. Kavousi, M.A. Zaeem, Quantitative phase-field modeling of solute trapping in rapid solidification, Acta Mater. 205 (2021) 116562.
[41] Y. Yang, S. Luo, P. Wang, W. Wang, M. Zhu, Multiphase field modeling of dendritic solidification of low-carbon steel with peritectic phase transition, Metall. Mater. Trans. B 52 (6) (2021) 3708–3719.
[42] J.S. Langer, H. Müller-Krumbhaar, Stability effects in dendritic crystal growth, J. Cryst. Growth 42 (1977) 11–14, https://doi.org/10.1016/0022-0248(77)90171-3
[43] W. Kurz, D.J. Fisher, Fundamentals of Solidification, fourth ed, Trans Tech Publications, Switzerland, 1998.
[44] A. Vondrous, M. Selzer, J. Hötzer, B. Nestler, Parallel computing for phase-field models, Int. J. High Perform. Comput. Appl. 28 (1) (2014) 61–72.
[45] J. Hötzer, M. Jainta, P. Steinmetz, B. Nestler, A. Dennstedt, A. Genau, M. Bauer, H. Köstler, U. Rüde, Large scale phase-field simulations of directional ternary eutectic solidification, Acta Mater. 93 (2015) 194–204, https://doi.org/10.1016/j.actamat.2015.03.051, http://www.sciencedirect.com/science/article/pii/S135964541500227X.
[46] M. Seiz, M. Kellner, B. Nestler, Simulation of dendritic–eutectic growth with the phase-field method, Acta Mater. 254 (2023) 118965.
[47] N.S. Bailey, K.-M. Hong, Y.C. Shin, Comparative assessment of dendrite growth and microstructure predictions during laser welding of al 6061 via 2D and 3D phase field models, Comput. Mater. Sci. 172 (2020) 109291.
[48] R. Trivedi, W. Kurz, Dendritic growth, Int. Mater. Rev. 39 (2) (1994) 49–74.
[49] S. Kou, Welding Metallurgy, John Wiley & Sons, Hoboken, New Jersey, 2003.
[50] M. Rappaz, C.-A. Gandin, Probabilistic modelling of microstructure formation in solidification processes, Acta Metall. Mater. 41 (2) (1993) 345–360.
[51] C.-A. Gandin, M. Rappaz, A coupled finite element-cellular automaton model for the prediction of dendritic grain structures in solidification processes, Acta Metall. Mater. 42 (7) (1994) 2233–2246.
[52] D. Walton, B. Chalmers, The origin of the preferred orientation in the columnar zone of ingots, Trans. Metall. Soc. AIME 215 (6) (1959) 1.
[53] J. Deschamps, M. Georgelin, A. Pocheau, Growth directions of microstructures in directional solidification of crystalline materials, Phys. Rev. E—Stat. Nonlinear Soft Matter Phys. 78 (1) (2008) 011605.
[54] C.A. Schneider, W.S. Rasband, K.W. Eliceiri, Nih image to imagej: 25 years of image analysis, Nat. Methods 9 (7) (2012) 671–675.
[55] L. Ren, S. Geng, P. Jiang, C. Han, J. Jin, Y. Wang, J. Wu, Multi-scale simulation of thermodynamic behavior and its effect on three-dimensional microstructure evolution in laser welds under different process parameters, Int. J. Heat Mass Transf. 256 (2026) 128064.
[56] H. Schönmaier, R. Krein, M. Schmitz-Niederau, R. Schnitzer, Influence of the heat input on the dendritic solidification structure and the mechanical properties of 2.25 cr-1mo-0.25 v submerged-arc weld metal, J. Mater. Eng. Perform. 30 (10) (2021) 7138–7151.
[57] H. Aghajani, M. Mosayebi, B. Pourbahari, S. Maleksaeedi, P. Alimehr, R. Esmaeilizadeh, M. Hasanabadi, N. Bassim, E. Toyserkani, Mechanistic process–microstructure–cracking correlations in laser powder bed fusion of the ni-based superalloy in738, Mater. Des. 262 (2026) 115504, https://doi.org/10.1016/j.matdes.2026.115504, https://www.sciencedirect.com/science/article/pii/S0264127526000742.
[58] E. Wasilewski, N. Doynov, R. Ossenbrink, V. Michailov, Investigations on the thermal conditions during laser beam welding of high-strength steel 100cr6, Adv. Ind. Manuf. Eng. 6 (2023) 100118.
[59] A. Gumenyuk, N. Bakir, M. Rethmeier, Two-colour thermography for measurement of temperature distribution in laser beam welding, Procedia CIRP 124 (2024) 468–471.
[60] D. Ushmaev, Z. Liao, A. Notron, D. Axinte, On the importance of interface stability in cellular automata models: planar and dendritic solidification in laser melted ysz, Mater. Des. 219 (2022) 110823, https://doi.org/10.1016/j.matdes.2022.110823, https://www.sciencedirect.com/science/article/pii/S0264127522004452.
[61] F. Qayyum, M. Umar, S. Guk, M. Schmidtchen, R. Kawalla, U. Prahl, Effect of the 3rd dimension within the representative volume element (RVE) on damage initiation and propagation during full-phase numerical simulations of single and multi-phase steels, Materials 14 (1) (2020) 42.
[62] D.K. Mendes Isidorio, J. da Cruz Payão Filho, M. Uddagiri, K. NouraniNiaki, O. Shchyglo, I. Steinbach, Super duplex stainless steel fabricated by arc-based directed energy deposition: microstructure evolution and phase field solidification simulation, Mater. Des. 254 (2025) 114027, https://doi.org/10.1016/j.matdes.2025.114027, https://www.sciencedirect.com/science/article/pii/S0264127525004472.